

# Disappointment aversion preferences and Option Pricing

Lerby M. Ergun<sup>\*</sup>

Bank of Canada

Bruno Feunou<sup>†</sup>

Bank of Canada

July 2025

## Abstract

The tendency of investors to weigh potential losses more heavily than gains plays a significant role in asset pricing. We develop a reduced-form dynamic model for the S&P500 return which follows a Gaussian-GARCH dynamic under the physical probability measure, and the pricing kernel blend together two components: (1) an exponential quadratic function of return component and (2) a disappointment aversion (DA) component. This pricing kernel transforms the Gaussian-GARCH model under the physical probability measure into a mixture of a truncated and standard Gaussian GARCH model under the risk-neutral probability measure. Leveraging this flexible setup to estimate the value of European-style call option contracts on the S&P 500, we find that adding a DA component to the pricing kernel reduces option pricing errors by approximately 20%.

---

<sup>\*</sup>lerbyergun@gmail.com, 234 Wellington Street West, Ottawa, ON, K1A 0G9, Canada.

<sup>†</sup>Corresponding author: BFeunou@bank-banque-canada.ca, 234 Wellington Street West, Ottawa, ON, K1A 0G9, Canada. We are grateful for comments from Jean-Sébastien Fontaine and seminar participants at the 2025 Quantact Thematic Day in Mathematical Finance (Montreal).

# 1 Introduction

Disappointment aversion (DA) plays a critical role in shaping investor behavior and has become an influential concept in asset pricing. In this expected utility framework, first introduced by [Gul \(1991\)](#), DA captures the idea that agents overweight outcomes that fall short of a reference point, leading to kinked utility functions. This distortion has direct implications for asset prices, particularly when investors face asymmetric risk. Given their strong sensitivity to investor preferences, option markets provide a powerful testing ground for DA. Yet, despite a rich literature on belief distortions and asymmetric preferences, few option pricing models explicitly incorporate DA into the pricing kernel.

In this paper, we propose a reduced-form option pricing framework that embeds DA into a dynamic stochastic discount factor. Our specification builds on [Christoffersen et al. \(2013\)](#) (henceforth CHJ) but introduces time-varying risk sensitivities and explicitly separates the DA contribution from the standard risk-neutral (RN) transformation. The model flexibly accommodates different GARCH specifications for the physical process, which processes have proven effective in capturing key empirical features of asset returns, such as volatility clustering and the leverage effect ([Bollerslev, 1986](#); [Engle and Ng, 1993](#)). As such, the model nests prior benchmark models as special cases. Importantly, the closed-form solution for one-day options enables clean identification of DA effects without interference from dynamic assumptions. This makes it possible to isolate and estimate investor preferences for the left and right sides of the distribution, relative to the DA threshold, directly from cross-sectional option prices.

Empirically, we find compelling evidence that DA contributes meaningfully to explaining option prices. For one-day options, the model reveals that investors tend to overweight the right tail, opposite to standard DA preferences. This aligns with findings by [Bryzgalova et al. \(2023\)](#), who show that retail traders dominate short-dated option volume and seek upside exposure.

When we extend the analysis to the full surface of options, DA substantially improves the model fit. We estimate three nested versions of the pricing kernel: (1) the benchmark model of CHJ, (2) a no-DA version that allows the price of return and variance risk to follow flexible dynamics, and (3) a fully flexible version that includes DA. By progressively relaxing the restrictions across these models, we demonstrate the incremental value of incorporating DA. In particular, DA enhances the model's ability to capture the shape of the implied volatility surface and improves the pricing of deep out-of-the-money options. Overall, incorporating DA reduces the vega-weighted root mean squared error (VWRMSE) by approximately 20%, with the majority of the improvement attributable to the DA component. These results underscore the importance of modeling preferences beyond return and variance, especially in capturing investor behavior across different regions of the distribution.

We also uncover meaningful time variation in DA sensitivity. The inferred parameters display rich dynamics over time and across maturities, consistent with changing macro-financial conditions. The estimated time-variation of sensitivity to disappointment is consistent with the findings of [Schreindorfer and Sichert \(2025\)](#). Pricing kernel estimates show that negative stock market returns are significantly more painful to investors in low-

volatility periods. Moreover, we document a term structure in DA aversion: shorter-dated options exhibit opposite preference patterns than medium- to longer-term options. These findings support the idea that investor horizons shape how DA manifests in market prices.

Our contributions are threefold. First, we introduce a reduced-form option pricing model that embeds DA into a GARCH-based framework. Our model flexibly accommodates various physical dynamics and features a pricing kernel with time-varying sensitivities to the return, volatility, and DA through conditional parameters. This builds on [Christoffersen et al. \(2013\)](#) and connects to structural models such as [Routledge and Zin \(2010\)](#); [Bonomo et al. \(2011\)](#) and [Ang et al. \(2005\)](#). A key advantage is the derivation of a closed-form solution for one-day options, allowing for clean identification of investor preferences directly from cross-sectional data. We extend the insights of structural models such as [Babiarz \(2024\)](#) and [Schreindorfer \(2020\)](#) by providing a reduced-form estimation framework that allows the data to reveal the presence and intensity of DA. This empirical approach complements their theoretical contributions and yields new insights into when and how such preferences shape option prices.

Second, we allow the pricing kernel to transform Gaussian physical distributions into skewed and truncated RN distributions. This departs from the standard practice of using exponentially linear pricing kernels ([Duffie et al., 2000](#)), which typically preserve distributional forms. Our specification, based on kinked utility functions, introduces discontinuities that break this symmetry. Despite these nonlinearities, we retain tractability by deriving an analytical solution for one-day option prices. In line with [Babaoglu et al. \(2018\)](#), we show that non-trivial transformations of the physical distribution are essential to improve option pricing accuracy. This feature enables us to distinguish how much of the skewness in observed option prices arises from investor preferences rather than return dynamics under the physical measure.

Third, our empirical results provide novel insights into how DA varies across time and investor horizons. For one-day options, we find that investors overweight right-side outcomes. This behavior contrasts with standard disappointment aversion and aligns with the findings of [Bryzgalova et al. \(2023\)](#), who document speculative behavior among retail traders in short-dated options. Similarly, [Adams et al. \(2024\)](#) find that, on the day of expiration, customer order imbalances for out-of-the-money SPX call options are more than double those for out-of-the-money put options. In contrast, medium-term investors exhibit disappointment-averse behavior, with DA reducing the vega-weighted RMSE by roughly 20%. These results demonstrate that preferences vary by investment horizon and state, and that DA plays a central role in shaping RN distributions. Furthermore, our framework contributes to the literature on higher-order risk preferences ([Harvey and Siddique, 2000](#); [Ang et al., 2006](#); [Feunou et al., 2013](#)).

Our work is related to the large body of GARCH option pricing models that capture time-varying volatility and non-normal return dynamics, including [Heston and Nandi \(2000\)](#); [Christoffersen and Jacobs \(2004\)](#); [Christoffersen et al. \(2006\)](#) and [Christoffersen et al. \(2010\)](#). While these models typically assume smooth, exponentially affine pricing kernels, our approach explicitly incorporates DA into the pricing kernel through a reduced-form yet flexible framework. Likewise, studies such as [Bates and Craine \(1999\)](#), [Maheu and McCurdy \(2004\)](#), and [Bégin et al. \(2020\)](#) focus on jump risk, news shocks,

or idiosyncratic volatility to explain risk premia but do not allow for preference-based distortions. Compared to more recent approaches like [Majewski et al. \(2015\)](#) and [Chorro and Fanirisoa Zazaravaka \(2022\)](#), which improve pricing accuracy through richer volatility or leverage dynamics, our model captures behavioral asymmetries through nonlinear investor preferences. By leveraging closed-form solutions for one-day options, we can isolate the DA contribution, providing a unique empirical window into how short- and medium-horizon investors differ in risk preferences.

The remainder of the paper is structured as follows. Section 2 outlines the theoretical framework, detailing the incorporation of DA into the RN measure. Section 3 describes the empirical methodology, where Section 4 describes the data and estimation techniques. Section 5 presents the results, comparing the performance between the nested models. Finally, Section 6 concludes.

## 2 Preferences and disappointment aversion

Our pricing kernel is derived from an equilibrium, consumption-based setting with a representative investor who has a rational DA utility function as introduced by [Gul \(1991\)](#). The investor evaluates uncertain future payoffs with a kinked utility function that penalizes realizations falling below a reference point.

The recursive utility is given by:

$$V_t = (1 - \delta)A_t + \delta R_t(V_{t+1}),$$

where  $A_t$  denotes current consumption,  $\delta$  is the time discount factor, and  $R_t(V_{t+1})$  is the certainty equivalent of future utility.

Under DA, the certainty equivalent is implicitly defined by:

$$\frac{R^{1-\gamma} - 1}{1 - \gamma} = \int \frac{V^{1-\gamma} - 1}{1 - \gamma} dF(V) - \left(\frac{1}{\alpha} - 1\right) \int_{V < R} \left(\frac{R^{1-\gamma} - V^{1-\gamma}}{1 - \gamma}\right) dF(V),$$

where  $\gamma$  is the relative risk aversion parameter,  $\alpha \in (0, 1]$  is the DA parameter, and  $F(V)$  is the distribution of continuation utilities. When  $\alpha = 1$ , the second integral vanishes, and preferences reduce to standard expected utility. When  $\alpha < 1$ , outcomes below the certainty equivalent  $R$  are weighted more heavily, reducing its value and reflecting a penalty for disappointment.

The pricing kernel is derived as the marginal rate of substitution between consumption at times  $t$  and  $t+1$ , adjusted for DA. Let  $R_{t+1}$  be the gross return on a consumption-claiming asset, then the one-period pricing kernel  $\text{SDF}_{t,t+1}$  is:

$$\text{SDF}_{t,t+1} = \delta (\delta R_{t+1})^{-\gamma} \cdot w(R_{t+1}), \quad (1)$$

where  $w(R_{t+1})$  captures the asymmetry in weighting gains versus losses:

$$w(R_{t+1}) = \begin{cases} \frac{1}{\mathbb{E}_t[\mathbb{I}(R_{t+1} < 1/\delta) + \alpha \mathbb{I}(R_{t+1} \geq 1/\delta)]} & \text{if } R_{t+1} < 1/\delta, \\ \frac{\alpha}{\mathbb{E}_t[\mathbb{I}(R_{t+1} < 1/\delta) + \alpha \mathbb{I}(R_{t+1} \geq 1/\delta)]} & \text{if } R_{t+1} \geq 1/\delta, \end{cases} \quad (2)$$

where  $\mathbb{I}(\cdot)$  is the indicator function. Plugging (2) into (1), the stochastic discount factor is compactly written as following:

$$\begin{aligned} \text{SDF}_{t,t+1} &= \delta (\delta R_{t+1})^{-\gamma} \cdot \left[ \frac{\mathbb{I}(R_{t+1} < 1/\delta) + \alpha \mathbb{I}(R_{t+1} \geq 1/\delta)}{\mathbb{E}_t[\mathbb{I}(R_{t+1} < 1/\delta) + \alpha \mathbb{I}(R_{t+1} \geq 1/\delta)]} \right] \\ &= \delta (\delta R_{t+1})^{-\gamma} \cdot \left[ \frac{1 + \left(\frac{1}{\alpha} - 1\right) \mathbb{I}(R_{t+1} < 1/\delta)}{1 + \left(\frac{1}{\alpha} - 1\right) \mathbb{E}_t[\mathbb{I}(R_{t+1} < 1/\delta)]} \right]. \end{aligned} \quad (3)$$

This pricing kernel tilts the RN measure in favor of downside states, consistent with evidence from option markets showing relatively high prices for crash protection. It introduces a kink at the disappointment threshold, generating asymmetric pricing of upside and downside risks. Notably, when  $\alpha < 1$ , downside outcomes receive higher weight in pricing, producing fatter left tails in the RN distribution.

## 2.1 A new reduced-form pricing kernel

The theoretical pricing kernel in equation (3), derived from DA preferences, serves as the foundation for the following specification of our reduced-form pricing kernel,  $PK_{t+1}$ :

$$PK_{t+1} = \frac{\widetilde{PK}_{t+1}}{\mathbb{E}_t[\widetilde{PK}_{t+1}]}, \quad \widetilde{PK}_{t+1} = \exp(\gamma_{1t} r_{t+1} + \gamma_{2t} r_{t+1}^2) \cdot (1 + \gamma_{3t} \cdot \mathbb{I}[r_{t+1} < -\kappa_t]), \quad (4)$$

where  $r_{t+1}$  is the log-return, that is  $r_{t+1} \equiv \ln R_{t+1}$ .

Our specification mimics (3), but is more flexible. A straightforward comparison between equations (3) and (4) enables us to ground our specification with the theory. Starting with our reduced-form disappointment threshold,  $\kappa_t$ . We have  $\kappa_t \equiv \log(\delta)$ , which links our reduced-form disappointment threshold to the agent's rate of time preference. However, in our empirical implementation, we treat  $\kappa_t$  as a flexible threshold chosen to best fit the data.  $\gamma_{3t}$  is our reduced-form DA parameter, indeed equating equations (3) and (4), one can easily establish that  $\gamma_{3t} \equiv \frac{1}{\alpha} - 1$ . However, we depart from the assumption of constant disappointment aversion and allow it to vary over time, an essential contribution of this paper.

Equating equations (3) and (4), reveals that  $\gamma_{1t}$  is the opposite of the relative risk aversion parameter:  $\gamma_{1t} \equiv -\gamma$ . However, we depart from the assumption of constant relative risk aversion and instead allow  $\gamma_{1t}$  to vary over time. Following [Christoffersen et al. \(2013\)](#), we extend Equation (3) by including the squared log return,  $r_{t+1}^2$ , in our reduced-form pricing kernel (4). The coefficient  $\gamma_{2t}$  captures sensitivity to variation of squared returns and, in the absence of DA, reflects the wedge between the conditional RN and physical variances. A quadratic log-pricing kernel can be linked to an important property that all admissible utility functions must have: non-increasing absolute risk aversion. As shown by [Kimball \(1990\)](#),  $\gamma_{2t}$  is closely associated with the concept of “relative prudence”, the investor's tendency to prepare or hedge in the face of uncertainty. This contrasts with “risk aversion,” which reflects the extent to which an investor dislikes uncertainty and seeks to avoid it.

Our reduced-form specification of the pricing kernel (4) departs from the exponentially affine class in [Duffie et al. \(2000\)](#), because of the nonlinear indicator term, which introduces a discontinuity at  $-\kappa_t$ . This discontinuity reflects the investor's kinked utility

response when returns fall below the disappointment threshold. Notably, our specification nests several common benchmarks: Setting  $\gamma_{2t} = \gamma_{3t} = 0$  recovers the logarithmic linear pricing kernel in the GARCH option pricing model of [Heston and Nandi \(2000\)](#). The vast majority of pricing kernel specifications in the GARCH option pricing literature correspond to this case. Setting  $\gamma_{3t} = 0$  yields the smooth pricing kernel used in [Christoffersen et al. \(2013\)](#), where return shocks affect prices in linear and quadratic terms. However, in their specification,  $\gamma_{2t}$  is inversely proportional to the physical variance, resulting in a constant ratio between the physical and risk-neutral variance. Importantly, our model allows the three preference components, risk aversion ( $\gamma_{1t}$ ), volatility aversion ( $\gamma_{2t}$ ) and DA ( $\gamma_{3t}$ ), to vary over time in an unrestricted manner. This flexibility enables the pricing kernel to generate a wider range of RN distributions that better align with observed option prices.

A discontinuity in the pricing kernel might not be a desired property as two return outcomes on both sides, and arbitrary closed, of the threshold ( $-\kappa_t$ ) have potentially very different discounting. One way to mitigate this is to approximate  $\mathbb{I}[r_{t+1} < -\kappa_t]$  with the following continuous function:

$$\mathbb{I}[r_{t+1} < -\kappa_t] \approx 1 - \Phi\left(\frac{r_{t+1} + \kappa_t}{\sigma}\right) - \frac{\sigma}{r_{t+1} + \kappa_t} \phi\left(\frac{r_{t+1} + \kappa_t}{\sigma}\right),$$

where  $\Phi(\cdot)$  and  $\phi(\cdot)$  denote standard normal cdf and pdf, respectively, and  $\sigma > 0$  is a smoothing parameter. This approximation has been widely used in the term structure of interest rate literature to model the link between the central bank target interest rate and the shadow rate. As shown in [Wu and Xia \(2016\)](#),  $1 - \Phi\left(\frac{s}{\sigma}\right) - \frac{\sigma}{s} \phi\left(\frac{s}{\sigma}\right)$  converges to  $\mathbb{I}[s < 0]$  as  $\sigma$  approaches 0. Our empirical investigation reveals no difference between using the indicator function and its continuous approximation. We therefore focus on our pricing kernel specification given in (4).

## 2.2 Preliminary evidence

Option data can provide insight into the key components that shape the pricing kernel. Provided a sufficiently wide range of strike prices for a given time to expiration, [Breedon and Litzenberger \(1978\)](#) show that the RN distribution can be recovered. By comparing the RN distribution to a physical benchmark, one can infer the shape of the pricing kernel and assess whether its features align with those predicted by our model, particularly in terms of risk aversion, volatility aversion, and DA. This section documents these features in the data and serves as a preliminary validation of the empirical relevance of the model structure.

Using CBOE intraday option pricing data, we fit a smooth spline to the mid-prices of put options across strike prices.<sup>1</sup> The RN density for a given day and maturity is then obtained by taking the second difference of the fitted put price curve across the integer strike prices.

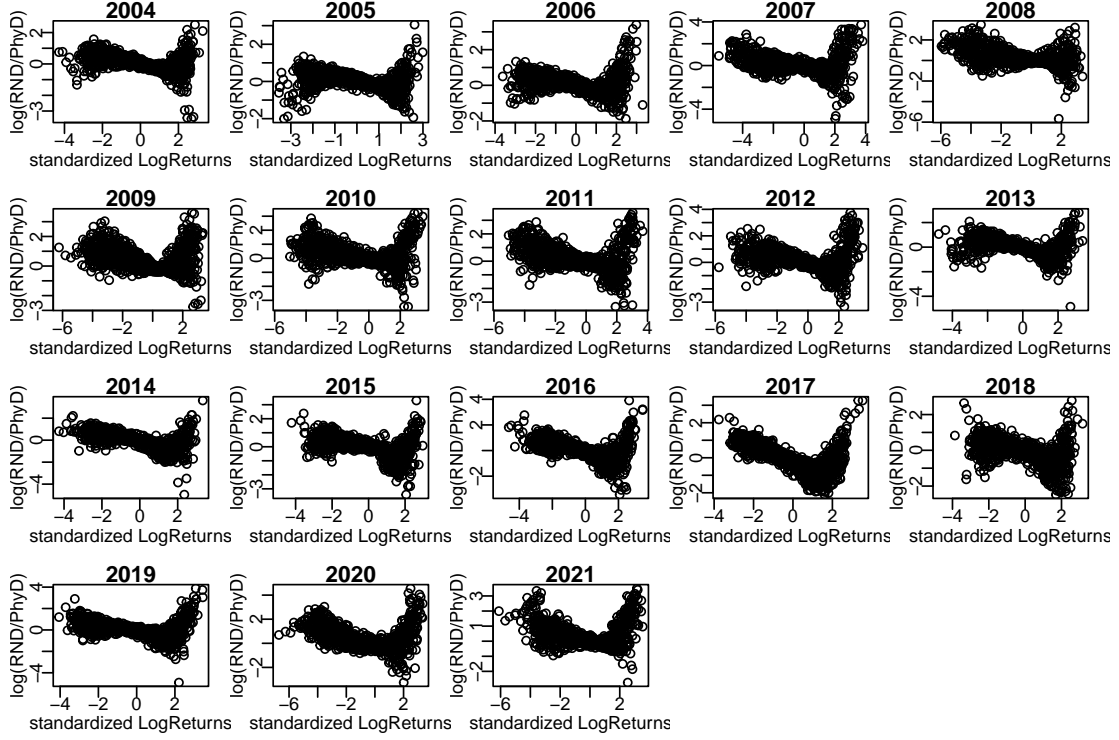
The physical distribution is generated by an EGARCH (2,2) model with a mean ARMA (2,2) process, which captures key characteristics of financial return series such as volatility

---

<sup>1</sup>See Appendix [A.5](#) for more details.

clustering, fat tails, and asymmetric volatility responses to negative shocks.<sup>2</sup> These models are also computationally convenient for simulating multi-horizon return distributions (see, e.g., [Bollerslev \(1986\)](#) and [Duffee \(1995\)](#)). Given the specified stochastic process, the ratio of the RN density to the physical density yields the pricing kernel. Figure 1 illustrates the resulting logarithmic pricing kernel using option prices from 2004 and 2021.

Figure 1: Pricing kernel extracted from option prices



These figures display the log of the ratio between the RN and physical return densities, interpreted as the log pricing kernel. The RN densities are inferred from CBOE option data using options with maturities between 25 and 35 days, following [Breedon and Litzenberger \(1978\)](#) by applying a second difference to a smooth spline fitted to put option prices. The physical densities are constructed by estimating an EGARCH(2,2) with an in-mean ARMA(2,2) model on SPX returns and simulating the conditional return distribution for the corresponding maturity. The simulated returns are binned into 50 equally sized intervals to approximate the density. Return quantiles are standardized by the simulated distribution's standard deviation. For presentation, 1,000 pricing kernel observations are randomly sampled for each year from 2004 to 2021, based on data collected each Wednesday.

The pricing kernel, defined as the log ratio of the RN and physical return densities, reveals several distinct patterns when visualized across different years. One consistent feature is the characteristic U-shape, which reflects the pricing kernel's convexity in return space. This motivates the inclusion of a squared return term, as in [Christoffersen et al. \(2013\)](#), to account for the heightened sensitivity to tail events. Additionally, there is notable variation in the shape and steepness of the pricing kernel over time, suggesting changes in attitudes toward risk and asymmetries in market beliefs. While the left side of the pricing kernel is often steeper, consistent with stronger pricing of downside risk, there is also substantial variation in the right tail, which is sometimes surprisingly steeply upward

<sup>2</sup>Results are robust to using alternative specifications such as the standard GARCH(2,2) and GJR-GARCH(2,2) models with ARMA(2,2) specification for the mean process.



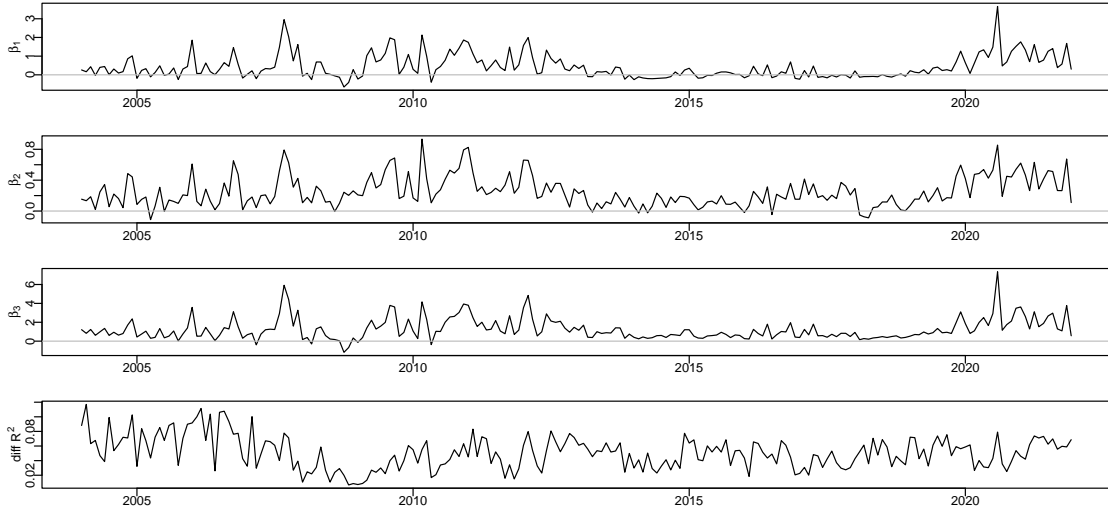
sloping. This asymmetry between negative and positive outcomes further motivates the inclusion of the indicator function that captures DA.

To better understand the components driving the shape of the pricing kernel, we run daily regressions of the pricing kernel at different quantiles on the components in Equation (4). We take the logarithm of the empirical pricing kernel and approximate the nonlinear term  $\log(1 + \gamma_{3t}\mathbb{I}[r_{i,t}^r < -\kappa_t])$  using a Taylor expansion. This yields the following regression specification:

$$\log(PK_i) = \beta_0 + \beta_1 r_i^* + \beta_2 (r_i^*)^2 + \beta_3 \mathbb{I}[r_i^* < -\kappa^*] + \epsilon_i, \quad (5)$$

where  $r_i^*$  denotes the return quantile  $i$  standardized by the standard deviation of the physical distribution for a given day, and  $\mathbb{I}[r_i^* < -\kappa^*]$  captures the presence of DA past the standardized threshold  $-\kappa^*$ .

Figure 2: Regression coefficients pricing kernel



These figures display the coefficient estimates from the regressions described in Equation (5). Each day, we regress the logarithm of the empirical pricing kernel, extracted from SPX options with maturities closest to 30 days, on a constant, the standardized return  $r_i^*$ , its square  $r_i^{*2}$ , and a DA indicator. The estimated coefficients are averaged within each month and plotted. The fourth panel shows the incremental explanatory power of the DA component, measured as the difference in  $R^2$  between the full regression in Equation (5) and a restricted version that excludes the DA term. The physical densities are constructed by estimating an EGARCH(2,2) model with an in-mean ARMA(2,2) specification on SPX returns, and simulating the corresponding conditional return distribution. Simulated returns are grouped into 50 equally sized intervals to approximate the density, and return quantiles are standardized by the standard deviation of the simulated physical distribution. The RN densities are derived from CBOE option data using contracts with closest to 30 day for that date, following [Breen and Litzenberger \(1978\)](#). The threshold  $-\kappa^* = 0$ .

Figure 2 shows the monthly averaged daily coefficient estimates of  $\beta_1$ ,  $\beta_2$  and  $\beta_3$ . First, the coefficients on the linear and squared return terms ( $r^*$  and  $r^{*2}$ ) are positive in most years, especially in more recent periods. This reinforces the characteristic U-shape of the log pricing kernel. As seen in Table 8 in the Appendix, the squared return term is almost always significant, consistent with [Christoffersen et al. \(2013\)](#), who emphasize that investors respond not just to the direction but also to the magnitude of returns.



The DA indicator is positive over nearly the whole time period, indicating that downside events below the disappointment threshold are systematically priced more aggressively. The magnitude of the DA coefficient varies notably across years, with particularly elevated levels in 2007 and 2011 years associated with heightened macro-financial stress during the onset of the global financial crisis and the euro area sovereign debt crisis, respectively. The strength of the DA effect in these periods suggests that investors placed substantial weight on downside risk beyond what is captured by return and volatility alone. Figure 16 in Appendix A.7 shows the corresponding t-statistics of the daily regression. They show that even in relatively calm periods, the DA coefficient remains statistically significant, pointing to a persistent premium on negative outcomes. This robustness indicates that DA is not merely episodic, but an important component of the pricing kernel across a wide range of market conditions.

The last panel of the figure displays the increase in adjusted  $R^2$  from including the DA component, measured relative to a restricted regression that omits the indicator function. The contribution of the DA term varies between 2% and 10%, indicating a meaningful and time-varying role in shaping of the pricing kernel. Given that the average  $R^2$  of the restricted model is around 60%, this improvement is substantial at times.<sup>3</sup>

### 3 Model

To evaluate the implications of DA for option pricing, we first specify the data generation process for asset returns under the physical probability measure.

#### 3.1 Dynamic under the physical probability measure

We break down the log returns of the underlying asset as following:

$$r_{t+1} = \ln \left( \frac{S_{t+1}}{S_t} \right) = e_t + \sqrt{h_t} z_{t+1}, \quad (6)$$

where  $z_{t+1} \sim^{\mathbf{P}} \mathcal{N}(0, 1)$  are i.i.d. standard normal shocks under the physical probability measure (which we denote by  $\mathbf{P}$ ). Hence  $h_t$  is the one-period ahead conditional variance and  $e_t$  the one-period ahead conditional mean under the physical probability measure  $\mathbf{P}$ , that is:

$$\begin{aligned} e_t &= E_t^{\mathbf{P}} [r_{t+1}] \\ h_t &= E_t^{\mathbf{P}} [(r_{t+1} - e_t)^2]. \end{aligned}$$

Both  $e_t$  and  $h_t$  vary over time, and our framework supports any GARCH-type specification for  $e_t$  and  $h_t$ : that is, innovations in  $e_{t+1}$  and  $h_{t+1}$  are functions of  $z_{t+1}$ .

#### 3.2 RN distribution

Given the physical dynamic of log-return, defined by (6), and the pricing kernel in Equation (4), we now derive the implied distribution under the RN measure (which we denote

---

<sup>3</sup>Figure 15 in Appendix A.7 presents similar results based on a nonlinear specification, where an additional parameter is introduced for the squared return term, that is,  $(r_i^* - a)^2$ . Furthermore, Table 8 in Appendix A.6 reports the results of annual regressions that pool daily data by year and include time-fixed effects to account for temporal variation.

by  $\mathbf{Q}$ ).

The starting point is the expected value of the stochastic discount factor  $\widetilde{PK}_{t+1}$  under  $\mathbf{P}$ . We establish that:

$$\begin{aligned} E_t^{\mathbf{P}} [\widetilde{PK}_{t+1}] &= E_t^{\mathbf{P}} [\exp(\gamma_{1t}r_{t+1} + \gamma_{2t}r_{t+1}^2)] + \gamma_{3t}E_t^{\mathbf{P}} [\exp(\gamma_{1t}r_{t+1} + \gamma_{2t}r_{t+1}^2) 1_{[r_{t+1} < -\kappa_t]}] \\ &= (1 + \gamma_{3t}\Phi(C_t)) E_t^{\mathbf{P}} [\exp(\gamma_{1t}r_{t+1} + \gamma_{2t}r_{t+1}^2)] \\ &= (1 + \gamma_{3t}\Phi(C_t)) \frac{1}{\sqrt{1 - 2h_t\gamma_{2t}}} \exp\left(\frac{2\gamma_{2t}e_t^2 + 2\gamma_{1t}e_t + h_t\gamma_{1t}^2}{2(1 - 2\gamma_{2t}h_t)}\right). \end{aligned}$$

To characterize the distribution of  $r_{t+1}$  under  $\mathbf{Q}$ , we compute the moment generating function (MGF) under  $\mathbf{Q}$ . We show in the appendix that:

$$\begin{aligned} E_t^{\mathbf{Q}} [\exp(ur_{t+1})] &= E_t^{\mathbf{P}} [PK_{t+1} \exp(ur_{t+1})] = \frac{E_t^{\mathbf{P}} [\widetilde{PK}_{t+1} \exp(ur_{t+1})]}{E_t^{\mathbf{P}} [\widetilde{PK}_{t+1}]} \\ &= \left( \frac{1 + \gamma_{3t}\Phi\left(C_t - \sqrt{\bar{h}_t}u\right)}{1 + \gamma_{3t}\Phi(C_t)} \right) \exp\left(a_{1t}u + \frac{\bar{h}_t}{2}u^2\right), \end{aligned} \quad (7)$$

where

$$\bar{h}_t \equiv \frac{h_t}{1 - 2h_t\gamma_{2t}}, \quad a_{1t} = \left(\gamma_{1t} + \frac{e_t}{h_t}\right) \bar{h}_t, \quad C_t = -\frac{\kappa_t + a_{1t}}{\sqrt{\bar{h}_t}}. \quad (8)$$

At this stage few important remarks can be made. Firstly, setting  $\gamma_{3t} = 0$  implies that  $r_{t+1} \sim^{\mathbf{Q}} \mathcal{N}(a_{1t}, \bar{h}_t)$ . Hence  $a_{1t}$  and  $\bar{h}_t$  are respectively the conditional risk-neutral expectation and variance of stock return in a world where DA is absent in the discounting factor. In the presence of DA, the risk-neutral distribution of  $r_{t+1}$  is no longer Gaussian. It displays deviations from normality, the extent of which depends on the strength of investor disappointment aversion,  $\gamma_{3t}$ , and the location of the disappointment threshold,  $\kappa_t$ . One obvious implication is that the risk-neutral skewness is different from zero. Beside, there are subtle deviations between the risk-neutral mean and variances and  $a_{1t}$  and  $\bar{h}_t$ . These deviations are function of the size of investor DA,  $\gamma_{3t}$ , and the disappointment threshold,  $\kappa_t$ . Given that we have derived the closed-form risk-neutral MGF in Equation (7), we can compute derivatives at any desired order to study the effect of DA on risk-neutral moments. In Appendix A.2 we have computed analytically the first, second, third, and fourth RN moments. We use these to illustrate the flexibility of the pricing kernel in shaping the distribution of returns.

### RN distribution: In between DA and the physical world

To better understand the effect of DA in our model, it is instructive to decompose the pricing kernel into two components: a standard RN transformation and an adjustment for DA. We implement this by introducing an intermediate probability measure, denoted  $\mathbf{Q}^{nd}$ , representing a RN world in which investor preferences are driven solely by traditional risk and volatility aversion, i.e., without DA.

The transformation from the physical measure to this baseline RN measure  $\mathbf{Q}^{nd}$  is done using the following pricing kernel:

$$PK_{t+1}^{\mathbf{P} \rightarrow \mathbf{Q}^{nd}} = \frac{\exp(\gamma_{1t}r_{t+1} + \gamma_{2t}r_{t+1}^2)}{E_t^{\mathbf{P}}[\exp(\gamma_{1t}r_{t+1} + \gamma_{2t}r_{t+1}^2)]}. \quad (9)$$

This kernel resembles the one used in [Christoffersen et al. \(2013\)](#), and preserve the Gaussian distribution under the  $\mathbf{Q}^{nd}$  probability measure, indeed we have

$$\begin{aligned} E_t^{\mathbf{Q}^{nd}}[\exp(ur_{t+1})] &= E_t^{\mathbf{P}}[PK_{t+1}^{\mathbf{P} \rightarrow \mathbf{Q}^{nd}} \exp(ur_{t+1})] \\ &= \exp\left(a_{1t}u + \frac{\bar{h}_t}{2}u^2\right), \end{aligned}$$

which implies that under  $\mathbf{Q}^{nd}$  the log return  $r_{t+1}$  is normally distributed with mean  $a_{1,t}$  and variance  $\bar{h}_t$ . Hence,

$$\begin{aligned} \gamma_{2t} &= \frac{1}{2} \left( \frac{1}{Var_t^{\mathbf{P}}[r_{t+1}]} - \frac{1}{Var_t^{\mathbf{Q}^{nd}}[r_{t+1}]} \right) \\ \gamma_{1t} &= \frac{E_t^{\mathbf{Q}^{nd}}[r_{t+1}]}{Var_t^{\mathbf{Q}^{nd}}[r_{t+1}]} - \frac{E_t^{\mathbf{P}}[r_{t+1}]}{Var_t^{\mathbf{P}}[r_{t+1}]}, \end{aligned}$$

implying that in the absence of DA,  $\gamma_{2t}$  measures the precision (inverse of the variance) spread between the physical and the RN distributions, while  $\gamma_{1t}$  measures the mean-to-variance-ratio spread between the risk-neutral and physical distributions.

DA enters as a second transformation, modifying the  $\mathbf{Q}^{nd}$ -distribution by applying an additional tilt that depends on whether the return  $r_{t+1}$  falls below a DA threshold  $-\kappa_t$ . Specifically, the adjustment from  $\mathbf{Q}^{nd}$  to the final RN measure  $\mathbf{Q}$  is governed by:

$$PK_{t+1}^{\mathbf{Q}^{nd} \rightarrow \mathbf{Q}} = \frac{1 + \gamma_{3t} \cdot \mathbb{I}[r_{t+1} < -\kappa_t]}{1 + \gamma_{3t} \cdot E_t^{\mathbf{Q}^{nd}}[\mathbb{I}[r_{t+1} < -\kappa_t]]}. \quad (10)$$

This kernel amplifies the weight placed on downside realizations when  $\gamma_{3t} > 0$ , effectively increasing the left-side density under  $\mathbf{Q}$  relative to  $\mathbf{Q}^{nd}$ .

The MGF of  $r_{t+1}$  under  $\mathbf{Q}$  can thus be expressed as follows:

$$\begin{aligned} E_t^{\mathbf{Q}}[\exp(ur_{t+1})] &= E_t^{\mathbf{Q}^{nd}}[PK_{t+1}^{\mathbf{Q}^{nd} \rightarrow \mathbf{Q}} \exp(ur_{t+1})] \\ &= \frac{E_t^{\mathbf{Q}^{nd}}[\exp(ur_{t+1})] + \gamma_{3t} E_t^{\mathbf{Q}^{nd}}[\exp(ur_{t+1}) \mathbb{I}[r_{t+1} < -\kappa_t]]}{1 + \gamma_{3t} E_t^{\mathbf{Q}^{nd}}[\mathbb{I}[r_{t+1} < -\kappa_t]]}. \end{aligned} \quad (11)$$

This decomposition provides a transparent interpretation of DA's contribution to the pricing kernel. Indeed, using (11), we can easily establish that

$$\gamma_{3t} = \frac{E_t^{\mathbf{Q}}[\mathbb{I}[r_{t+1} < -\kappa_t]] - E_t^{\mathbf{Q}^{nd}}[\mathbb{I}[r_{t+1} < -\kappa_t]]}{E_t^{\mathbf{Q}^{nd}}[\mathbb{I}[r_{t+1} < -\kappa_t]] E_t^{\mathbf{Q}}[\mathbb{I}[r_{t+1} > -\kappa_t]]},$$

hence the parameter  $\gamma_{3t}$  captures the additional distortion in the risk-neutral distribution, reallocating probability mass beyond what is explained by standard risk aversion

and volatility compensation. When  $\gamma_{3t} > 0$ , the model shifts more probability mass to the left side under  $\mathbf{Q}$ , increasing the value of downside protection. In this way, DA provides an intuitive and tractable channel through which the model captures observed option pricing asymmetries.

Through some straightforward math we show that  $E_t^{\mathbf{Q}^{nd}}[\mathbb{I}[r_{t+1} < -\kappa_t]] = \Phi(C_t)$ , and  $\Phi(C_t)$  is the  $\mathbf{Q}^{nd}$  probability of disappointment of the investor. There is a mapping between  $\kappa_t$  and  $C_t$ , and using Equation (8) we can express  $\kappa_t$  as a function of  $C_t$ :

$$-\kappa_t = C_t \sqrt{\text{Var}_t^{\mathbf{Q}^{nd}}[r_{t+1}]} + E_t^{\mathbf{Q}^{nd}}[r_{t+1}],$$

hence,  $C_t$  can thus be interpreted as the number of standard deviation of the  $\mathbf{Q}^{nd}$  distribution below which the investor is disappointed. For that reason, and for convenience, all our discussions throughout the rest of the paper are done by setting and varying  $C_t$ , in lieu of  $\kappa_t$ .

### RN distribution: Mixing a Gaussian with truncated Gaussian

An alternative and complementary interpretation of the pricing kernel is to view the implied RN distribution as a mixture of two Gaussian components: a full Gaussian distribution and a truncated Gaussian, with their relative weights governed by the DA parameter  $\gamma_{3t}$ .

Let  $\bar{r}_{t+1}$  denotes an hypothetical logarithmic return such that  $\bar{r}_{t+1} \sim^{\mathbf{Q}} \mathcal{N}(a_{1,t}, \bar{h}_t)$ . Then, the MGF of  $r_{t+1}$  under  $\mathbf{Q}$  can be expressed as:

$$E_t^{\mathbf{Q}}[\exp(ur_{t+1})] = \begin{cases} \rho_t \cdot g_{lt}^{\mathbf{Q}}(u) + (1 - \rho_t) \cdot g_t^{\mathbf{Q}}(u), & \text{if } \gamma_{3t} > 0, \\ \rho_t \cdot g_{ut}^{\mathbf{Q}}(u) + (1 - \rho_t) \cdot g_t^{\mathbf{Q}}(u), & \text{if } \gamma_{3t} \leq 0, \end{cases}$$

where  $g_t^{\mathbf{Q}}(u) \equiv E_t^{\mathbf{Q}}[\exp(u\bar{r}_{t+1})]$  is the MGF of Gaussian distribution with mean  $a_{1t}$  and variance  $\bar{h}_t$ . Furthermore,  $g_{lt}^{\mathbf{Q}}(u) \equiv E_t^{\mathbf{Q}}[\exp(u\bar{r}_{t+1}) \mid \bar{r}_{t+1} \leq -\kappa_t]$  is the MGF of the left side truncated normal distribution and  $g_{ut}^{\mathbf{Q}}(u) \equiv E_t^{\mathbf{Q}}[\exp(u\bar{r}_{t+1}) \mid \bar{r}_{t+1} > -\kappa_t]$  is the MGF of the right side truncated normal distribution. The weight  $\rho_t$  determines how much mass is shifted toward the truncated region and is defined as:

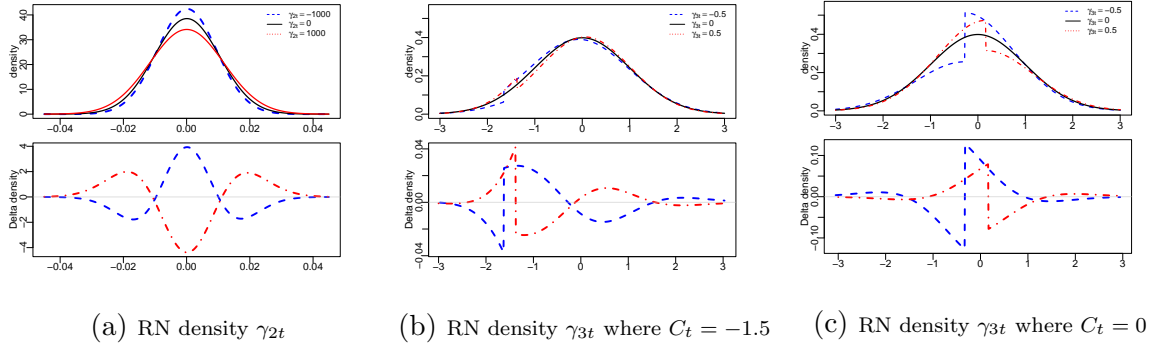
$$\rho_t = \begin{cases} \frac{\gamma_{3t}\Phi(C_t)}{1 + \gamma_{3t}\Phi(C_t)}, & \text{if } \gamma_{3t} > 0, \\ \frac{-\gamma_{3t}(1 - \Phi(C_t))}{1 + \gamma_{3t}\Phi(C_t)}, & \text{if } \gamma_{3t} \leq 0. \end{cases} \quad (12)$$

First, observe that when  $\gamma_{3t} = 0$ , the pricing kernel reduces to its standard Gaussian form. The left panels of Figure 3 illustrates how changes in  $\gamma_{2t}$  influence the shape of the risk-neutral distribution under this baseline. The upper left panel shows the densities for three values of  $\gamma_{2t}$ , while the lower panel highlights the displacement of the mass relative to the reference case  $\gamma_{2t} = 0$ . As  $\gamma_{2t}$  increases, the distribution becomes more dispersed, with the probability mass shifting symmetrically toward both tails, reflecting an increase in RN variance. In contrast, negative values of  $\gamma_{2t}$  compress the distribution, concentrating the probability around the center and reducing the likelihood of extreme outcomes.

While  $\gamma_{2t}$  governs symmetric variation in dispersion,  $\gamma_{3t}$  introduces asymmetric adjustments in the RN distribution. The central panel of Figure 3 further illustrates the effect of varying  $\gamma_{3t}$ , holding  $\gamma_{2t} = 0$  and fixing the RN variance to one. When  $\gamma_{3t} > 0$ , the mass is shifted to the left side of  $C_t$ , increasing the probability of negative outcomes under the RN measure. In contrast, for  $\gamma_{3t} < 0$ , the distribution flattens in the left tail, reallocating mass toward the center. Since the x-axis displays the demeaned, standardized quantile, the shift in the discontinuity observed between  $\gamma_{3t} = -0.5$  and  $\gamma_{3t} = 0.5$  in the lower panel indicates that the first moment of the RN distribution also changes.

The right panel of Figure 3 illustrates the role of  $t$  in shaping the RN distribution, shown here for the case  $C_t = 0$ . While  $\gamma_{3t}$  governs the intensity of the shift in the probabilities of the left side,  $t$  plays an equally important role in determining where this shift occurs. Its most direct effect is to control the location of the discontinuity in the RN density function. In addition,  $\kappa_t$  influences how sensitive the RN distribution is to changes in  $\gamma_{3t}$ , as seen by its effect on the weight  $\rho$  in (12). As a result, the discontinuity in the density becomes more pronounced as  $\kappa_t$  approaches zero.

Figure 3: RN density for  $\gamma_{2t}$  and  $\gamma_{3t}$



The figure depicts the RN densities for different values of  $\gamma_{2t}$  and  $\gamma_{3t}$ . In the left two panels, we set  $\gamma_{2t} \in \{-1000, 0, 1000\}$  with  $\gamma_{3t} = 0$ . In the middle and right panels, we fix  $\gamma_{3t} \in \{-0.5, 0, 0.5\}$  with  $C_t = 1.5$  and  $C_t = 0$ , respectively. Both the middle and right panels are demeaned, normalizing the first moment to zero. We use the mean fitted values from the physical process for  $h_t$  and  $e_t$ , which are inputs to  $a_t$ . For the right panel, we additionally set  $\gamma_{2t} = 0$  and fix the RN variance to one. The lower panels depict the change in density relative to the  $\gamma_{2t} = 0$  or  $\gamma_{3t} = 0$ .

## RN moments

Figure 4 provides a graphical representation of the RN moments, derived in Appendix A.2, as a function of  $\gamma_{3t}$  and  $C_t$ . The RN variance is normalized to one to facilitate interpretation of higher-order moments. For  $C_t = -1.5$ , increasing  $\gamma_{3t}$  shifts the probability mass to the left tail of the distribution, leading to a decline at the first moment. The second row of the figure shows  $\bar{h}_t$ , the RN variance in a world without DA. Because the threshold is located in the left tail,  $\gamma_{3t} > 0$  increases the RN variance relative to the no-DA baseline. Consequently, the third moment becomes increasingly negative, reflecting the asymmetric accumulation of mass in the left tail. Excess kurtosis also rises with higher values of  $\gamma_{3t}$ , capturing the fattening of both tails induced by the kink in the pricing kernel.

For  $C_t = 0$ , the behavior of the moments is more nuanced. In particular, the RN variance decreases relative to the no-DA RN variance,  $\bar{h}_t$ , as  $\gamma_{3t}$  deviates from zero, contrary to the case with  $C_t = -1.5$ . The skewness pattern also differs. At first glance, the changes in skewness appears counterintuitive: for  $\gamma_{3t} > 0$ , the distribution exhibits positive skewness despite the fact that DA penalizes negative outcomes. However, it is important to note that the first moment also changes concurrently, effectively shifting the RN distribution to the right when computing central moments. This shift places more mass in the right tail, as illustrated by the red line in the lower right panel of Figure 3. Although the resulting apparent change in the right tail is modest, it carries significant weight in the higher-order moments. This asymmetry turns the change in third moment positive, as the influence of the right tail dominates the initial accumulation of mass on the left near the center of the distribution.

Finally, for  $C_t = 1.5$ , increasing  $\gamma_{3t}$  causes more mass to shift toward the right side of the distribution, raising the first moment. Despite this directional shift, the skewness remains close to the levels observed when the threshold lies in the left tail, suggesting that the mass is displaced in a fairly symmetric way around the mean. In contrast, excess kurtosis decreases with higher  $\gamma_{3t}$ , moving opposite to the pattern observed with  $C_t = -1.5$ .

To summarize, the relationship between skewness and DA at different threshold locations, Figure 5 plots the skewness of the RN distribution for two fixed values of  $\gamma_{3t} \in \{-0.4, 0.4\}$ , as shown in Figure 4. The difference between the two lines can be interpreted as the slope of the skewness as a function of  $\gamma_{3t}$ . Skewness is downward sloped, as is the case for  $C_t = -1.5$ , when the threshold is placed more than one standard deviation away from the center of the distribution. These figures will help guide the interpretation of the RN moments extracted from the estimated model.

Overall, this interpretation shows that the model-implied RN return distribution is highly flexible. It can accommodate both positive and negative skewness, even when the physical return distribution is conditionally Gaussian. This flexibility allows for a disciplined identification of the influence of DA by separating the impact of the physical return dynamics from investor preferences.

### 3.3 No-arbitrage condition

In principle, the pricing kernel includes three free preference parameters:  $\gamma_{1t}$ ,  $\gamma_{2t}$ , and  $\gamma_{3t}$ . The no-arbitrage condition,  $E^Q[e^{r_{t+1}}] = e^{r_f}$ , imposes a restriction on their joint values. This implies that only two of the three parameters are free. For tractability, we opt to pin down  $\gamma_{3t}$  as a function of the other two parameters,  $\gamma_{1t}$ ,  $\gamma_{2t}$ :

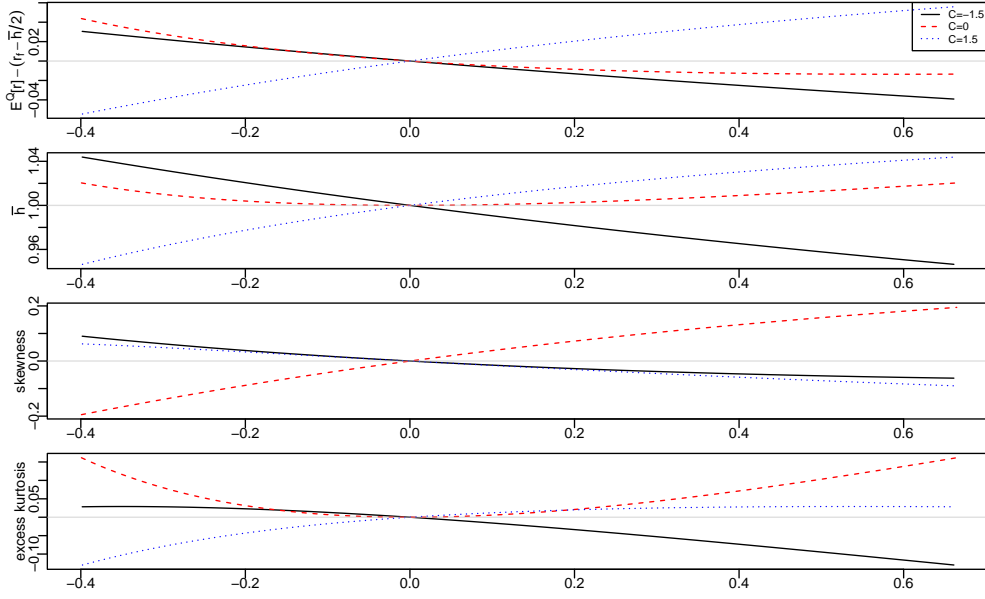
$$\gamma_{3t} = \frac{\exp(\bar{h}_t(\bar{\gamma}_{1t} - \gamma_{1t})) - 1}{\Phi(C_t - \sqrt{\bar{h}_t}) - \Phi(C_t) \cdot \exp(\bar{h}_t(\bar{\gamma}_{1t} - \gamma_{1t}))},$$

where

$$\bar{\gamma}_{1t} = \frac{r_f}{\bar{h}_t} - \frac{e_t}{h_t} - \frac{1}{2}. \quad (13)$$

In addition, to ensure a nonnegative pricing kernel at any given time  $t$ , it must be the case that  $\gamma_{3t} > -1$ , which implies a bound on  $\gamma_{1t}$ .

Figure 4: RN moments vs  $\gamma_{3t}$



The figure depicts the RN moments as a function of  $\gamma_{3t}$ , ranging from  $-0.4$  to  $0.7$ , with the second RN moment normalized to one. The top panel shows the first moment of the RN distribution corrected for the no-DA risk premium. The second panel plots  $\bar{h}$ . The third panel displays the skewness of the RN distribution, and the bottom panel shows its excess kurtosis. We use the average fitted values for  $h_t$  and  $e_t$  from the physical process as inputs. Additionally, we set  $C_t \in \{-1.5, 0, 1.5\}$  for the different lines in each panel.

Indeed, we show in the Appendix that  $\gamma_{3t} > -1$  if and only if

$$\hat{\gamma}_{1t}^l < \gamma_{1t} - \bar{\gamma}_{1t} < \hat{\gamma}_{1t}^u \quad (14)$$

where

$$\hat{\gamma}_{1t}^l \equiv \frac{1}{\bar{h}_t} \ln \left( \frac{\Phi(-C_t)}{\Phi(-C_t + \sqrt{\bar{h}_t})} \right), \quad \hat{\gamma}_{1t}^u \equiv \frac{1}{\bar{h}_t} \ln \left( \frac{\Phi(C_t)}{\Phi(C_t - \sqrt{\bar{h}_t})} \right).$$

To ensure that (14) holds, we re-parameterize  $\gamma_{1t}$  by expressing it as a function of a free parameter which we denote by  $\tilde{\gamma}_{1t}$

$$\gamma_{1t} = \bar{\gamma}_{1t} + \hat{\gamma}_{1t}^l \hat{\gamma}_{1t}^u \left( \frac{\exp(-\tilde{\gamma}_{1t}) - 1}{\hat{\gamma}_{1t}^u \exp(-\tilde{\gamma}_{1t}) - \hat{\gamma}_{1t}^l} \right).$$

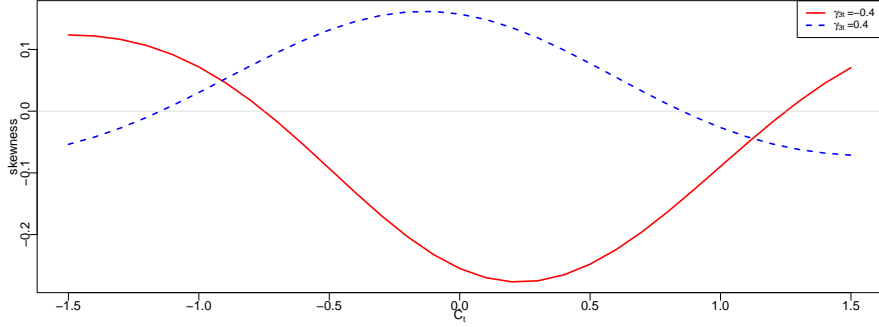
Note that  $\tilde{\gamma}_{1t} = 0$  is equivalent to  $\gamma_{3t} = 0$  and  $\gamma_{1t} = \bar{\gamma}_{1t}$ , and thus  $\tilde{\gamma}_{1t}$  can be interpreted as a restriction-free disappointment aversion parameter.

### 3.4 Model implied one-period option price

Most existing approaches rely on a log-linear pricing kernel or restrict the pricing kernel to simple transformations, such as shifts in the mean or adjustments to the second moment, see, e.g., Figure 3. Departing from these conventions introduces significant challenges, as the resulting nonlinearity makes it difficult to derive the RN distribution and complicates the fast evaluation of option values. Despite these complexities, we show that it is still possible to obtain a closed-form expression for the model-implied price of a one-day



Figure 5: Skewness vs  $C_t$



This figure depicts the skewness of the RN distribution for different values of the DA threshold  $C_t$ , conditional on a given  $\gamma_{3t}$ . The gap between the red and blue lines illustrates the sensitivity of skewness to changes in  $C_t$ , corresponding to the slope of the skewness curve with respect to the DA threshold in Figure 4.

option. Leveraging the GARCH dynamics of the physical return process and the non-smooth structure of the pricing kernel, we derive the call option price conditional on the model parameters.<sup>4</sup>

$$\begin{aligned}
 C_m(e_t, h_t, \gamma_{1t}, \gamma_{2t}) = & \\
 e^{-r_f} (1 + \gamma_{3t} \Phi(C_t))^{-1} & \left[ \Phi(\sqrt{h_t} - D_t) \tilde{S}_t - \Phi(-D_t) K \right] + \\
 \tilde{\gamma}_{3t} & \left[ \left( \Phi(C_t - \sqrt{h_t}) - \Phi(D_t - \sqrt{h_t}) \right) \tilde{S}_t - (\Phi(C_t) - \Phi(D_t)) K \right] \quad (15)
 \end{aligned}$$

where

$$D_t \equiv \frac{\ln\left(\frac{K}{S_t}\right) - a_{1,t}}{\sqrt{h_t}}, \quad \tilde{S}_t \equiv e^{-\bar{h}_t(2a_{1,t} + \bar{h}_t)} S_t \quad \text{and} \quad \tilde{\gamma}_{3t} \equiv \gamma_{3t} 1_{\left[\ln\left(\frac{K}{S_t}\right) < -\kappa_t\right]}.$$

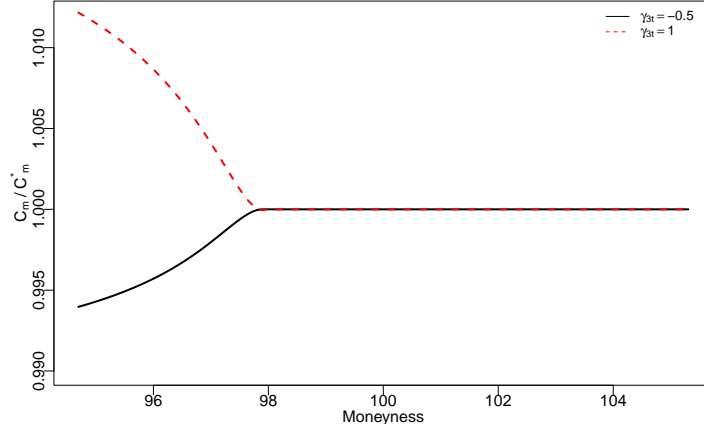
The closed form formula cleanly separates into a no DA part and DA part. The first part resembles the [Black and Scholes \(1973\)](#) option pricing model. The departure from the classical approach is illustrated in Figure 6. We plot the no DA option price relative to the DA option price for different levels of the moneyness of the option. One can clearly see that for  $\gamma_{3t} > 0$ , the options that insure against left tail events are more expensive relative to the non-DA counterpart. The opposite holds for  $\gamma_{3t} < 0$ , as seen from the black solid line. Given that the  $\gamma$ 's are allowed to vary over time, this DA framework is able to facilitate occasions where the sign might switch.

### 3.5 Dynamics

To obtain the multi-step ahead distribution, one must specify the dynamics governing both the physical and RN processes. As noted previously, any form of GARCH specification for  $h_t$  and  $e_t$  is admissible within our framework. For our main specification, we adopt the model of [Heston and Nandi \(2000\)](#), which has become the standard reference for GARCH-based option pricing. For robustness, we provide estimates with EGARCH dynamics.

<sup>4</sup>See Appendix A.3 for a detailed derivation.

Figure 6: Model implied option price vs  $\gamma_{3t}$



The figure shows the model implied option price relative to the option price with no DA, i.e.,  $C_m^*$ .  $C_m$  is the model implied option price with the  $\gamma_{3t}$  set to -0.5 and 1 for the solid and dashed line, respectively. The values for  $h_t$  and  $e_t$  we take the mean of the fitted values from the physical process. Furthermore,  $\bar{h}_t$  is set to 1.05 times the mean of  $h_t$  and  $C_t = -1.5$ .

### 3.5.1 Physical dynamic parameters

In our empirical implementation the variance evolves according to:

$$h_{t+1} = \beta_0 + \beta_1 h_t + \beta_2 \left( z_{t+1} - \theta \sqrt{h_t} \right)^2.$$

This GARCH structure captures volatility clustering through the autoregressive term and incorporates the leverage effect via the asymmetric shock term. An important feature of the [Heston and Nandi \(2000\)](#) setup is its compatibility with closed-form option pricing under log-linear pricing kernels. The model includes a risk premium in the conditional mean return and has been extended by [Christoffersen et al. \(2013\)](#) to also allow for a premium on return variance.

We further enrich the model by extending the specification of the conditional mean. First we decompose  $e_t$  in two components,  $e_t = \bar{e}_t + \tilde{e}_t$ , where  $\bar{e}_t$  is the expected return specification postulated in existing GARCH-option pricing papers:  $\bar{e}_t \equiv r_f + \lambda h_t - \frac{h_t}{2}$ . We depart from this commonly used expected-return, assuming potential persistent deviation between  $e_t$  and  $\bar{e}_t$ , that is  $\tilde{e}_t = e_t - \bar{e}_t$  is a mean-reverting AR(1) process:

$$\tilde{e}_{t+1} = \alpha_0 + \alpha_1 \tilde{e}_t + \alpha_2 \sqrt{h_t} z_{t+1}.$$

This structure reflects empirical evidence of the continuation of returns after large shocks (see [Calvet and Fisher, 2007](#)) and allows the model to better capture the interplay between volatility and expected returns.

### 3.5.2 Pricing Kernel parameters

Our framework is flexible and compatible with any type of GARCH-style dynamic for both  $\tilde{\gamma}_{1t}$  and  $\gamma_{2t}$ . We assume that  $\tilde{\gamma}_{1t}$  follows a simple AR(1) process, that is:

$$\tilde{\gamma}_{1t+1} = \bar{\alpha}_0 + \bar{\alpha}_1 \tilde{\gamma}_{1t} + \bar{\alpha}_2 z_{t+1}. \quad (16)$$

Furthermore, note that  $\gamma_{2t}$  captures the wedge between the physical conditional variance  $h_t$  and the no-DA risk-neutral variance  $\bar{h}_t$ , defined as

$$\gamma_{2t} = \frac{1}{2} \left( \frac{1}{h_t} - \frac{1}{\bar{h}_t} \right).$$

As a result, specifying a dynamic process for  $\gamma_{2t}$  is equivalent to specifying a dynamic process for  $\bar{h}_t$ :

$$\bar{h}_{t+1} = \bar{\beta}_0 + \bar{\beta}_1 \bar{h}_t + \bar{\beta}_2 \left( z_{t+1} - \bar{\theta} \sqrt{\bar{h}_t} \right)^2, \quad (17)$$

which mimics that of  $h_t$  as they are both variances.

### 3.5.3 Benchmark models

To evaluate the contribution of DA to option pricing, we estimate and compare three nested specifications of the pricing kernel. All models share a common physical process but have restrictions on the pricing kernel. The baseline model, CHJ, corresponds to the framework in [Christoffersen et al. \(2013\)](#), where there is no disappointment aversion ( $\gamma_{3t} = 0$ ) and the risk-neutral variance ( $\bar{h}_t$ ) is a fixed proportion of the physical variance ( $h_t$ ), that is  $\bar{h}_t = \left(\frac{\theta}{\bar{\theta}}\right)^2 h_t$ . The second specification, no DA, relaxes this proportionality by allowing a separate dynamic process for the risk-neutral variance, though it still excludes DA by setting  $\gamma_{3t} = 0$ . Finally, the most flexible model, DA, introduces time variation in both the linear and quadratic pricing kernel components and allows for disappointment aversion through a non-zero, time-varying  $\gamma_{3t}$ . This fully unrestricted specification captures the asymmetry and tail behavior in risk-neutral distributions that simpler models may miss. We summarize the different restriction imposed by each of these model in Table 1.

Table 1: Pricing Kernel Restrictions

Model	$\bar{\alpha}_0$	$\bar{\alpha}_1$	$\bar{\alpha}_2$	$\bar{\beta}_0$	$\bar{\beta}_1$	$\bar{\beta}_2$	$\bar{\theta}$
<b>CHJ</b>	0	0	0	$\left(\frac{\theta}{\bar{\theta}}\right)^2 \beta_0$	$\beta_1$	$\left(\frac{\theta}{\bar{\theta}}\right)^2 \beta_2$	NR
<b>no DA</b>	0	0	0	NR	NR	NR	NR
<b>DA</b>	NR	NR	NR	NR	NR	NR	NR

This table reports the pricing kernel parameter restrictions for the different models. NR indicates that there is no restriction.

### 3.5.4 Multi-period dynamics

Due to the non-affine nature of the RN dynamics implied by DA, closed-form expression for option prices with maturity higher than one are not available. Consequently, option values must be computed through simulation.

The first approach simulates returns directly under the full RN measure  $\mathbf{Q}$ , which incorporates DA at each horizon. This involves sampling from a mixture of Gaussian and truncated Gaussian distributions, with time-varying mixture weights. Although this method is fully aligned with the theoretical structure of the model, it is computationally demanding and less tractable, particularly when estimating model parameters.

A more efficient alternative is to simulate returns under the no-DA RN measure  $\mathbf{Q}^{nd}$ , where the dynamics are Gaussian. In this two-step approach, returns are generated under  $\mathbf{Q}^{nd}$  and then adjusted path-by-path using the pure DA pricing kernel described in Equation (10). This strategy avoids mixture sampling and is both computationally efficient and numerically stable.

Finally, a third method simulates returns under the physical measure  $\mathbf{P}$ , applying the full pricing kernel to reweigh simulated paths. While conceptually straightforward, this method tends to suffer from numerical instability, as the pricing kernel features nonlinear transformations that can vary substantially across both time and simulation paths.

The computational challenges posed by simulating directly under  $\mathbf{Q}$  or reweighting under  $\mathbf{P}$  motivated the development of a more computationally tractable alternative. The second approach, via  $\mathbf{Q}^{nd}$ , offers a favorable balance between numerical stability and consistency with the model’s structure, and is the method we adopt in this paper. Appendix A.4 provides full implementation details for all three simulation methods.

### 3.5.5 Model implied term structures

Figure 7 depicts the average wedge between the physical and RN variance and skewness across the term structure. The top-left panel shows that the behavior of the variance wedge varies by threshold. For  $C_t = -1.5$ , the wedge increases with  $\gamma_{3t}$ , highlighting the growing contribution of DA to RN variance. For  $C_t = 0$ , the wedge increases when  $\gamma_{3t}$  lies outside the approximate range  $[-0.2, 0]$ . This is consistent with Figure 3, which shows that the variance in the no-DA case is elevated whenever  $\gamma_{3t} \neq 0$ .<sup>5</sup> The pattern for the slope of the wedge is very similar to the average wedge over the term structure.

The bottom-left panel of Figure 7 presents the skewness wedge. In most cases, the wedge is positive for values of  $\gamma_{3t}$ . For  $C_t = 0$ , the relationship with  $\gamma_{3t}$  exhibits an S-shape around  $\gamma_{3t}$  close to zero, however with RN skewness exceeding physical skewness at both ends of the  $\gamma_{3t}$  range. For  $C_t = -1.5$ , the wedge increases with  $\gamma_{3t}$ , even though the one-period-ahead RN skewness is lower than the physical skewness for all values of  $\gamma_{3t}$ . A similar pattern appears in the bottom-right panel, which shows the slope of the skewness wedge. These results highlight the complexity of DA’s influence on the distribution of returns over longer horizons.

## 4 Estimation and data

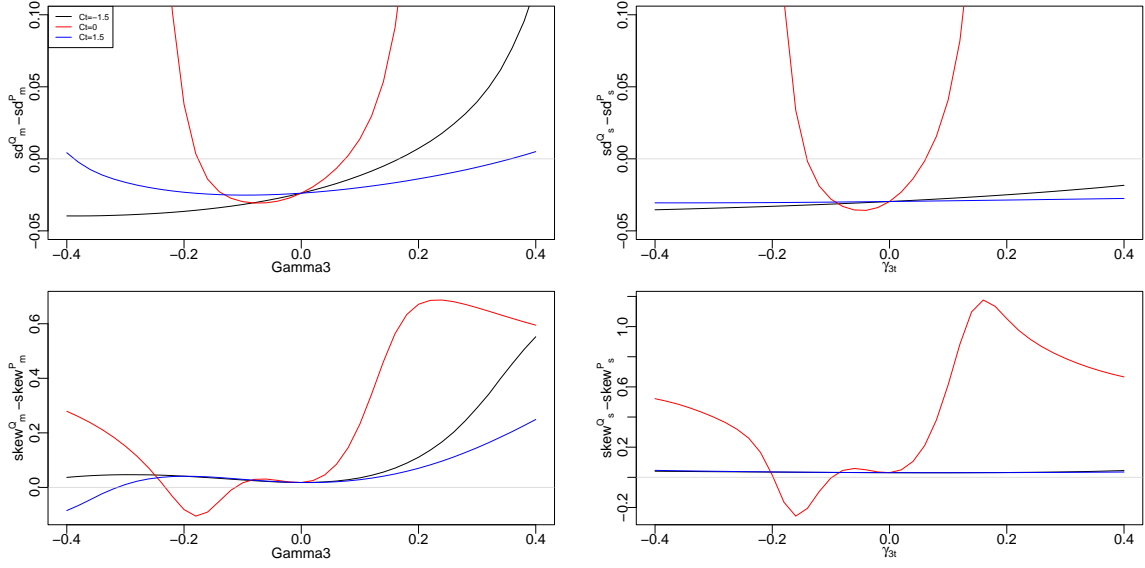
### 4.1 Estimation strategy

To estimate the structural parameters of our model, we follow the joint likelihood estimation approach, as in Christoffersen et al. (2013). This methodology combines information from both time-series returns and the cross-section of option prices, ensuring that the estimated parameters jointly reflect the physical and RN distributions.

---

<sup>5</sup>Figure 17 in the Appendix confirms that the steep U-shape is primarily driven by the difference between the DA and no-DA models, rather than by the indirect effect of  $\gamma_{3t}$  on  $\gamma_{1t}$ .

Figure 7: Term structure RN densities



(a) Difference in average

(b) Difference in slope

The figure depicts the wedge between the standard deviation and skewness of the RN and physical distributions over 180-day terms as a function of  $\gamma_{3t}$ . For this exercise  $\gamma_{2t}$  and  $\gamma_{3t}$  are constant, i.e.,  $\bar{\beta}_0 = \psi\beta_0$ ,  $\bar{\beta}_1 = \beta_1$ ,  $\bar{\beta}_2 = \psi\beta_2$ ,  $\bar{\theta} = \theta/\sqrt{\psi}$ ,  $\bar{\alpha}_1 = 0$  and  $\bar{\alpha}_2 = 0$ . The left panels show the average wedge across terms, while the right panels display the slope, measured as the difference between the 180-day and 1-day wedges. To simulate the physical distribution, we use an EGARCH(2,2)-in-mean(2,2) model, and the RN distribution is implied by our DA model. The results are shown for three different values of  $C_t = \{-1.5, 0, 1.5\}$ .

We specify a joint likelihood function composed of two components: a return likelihood based on the daily return distribution under the physical measure  $\mathbf{P}$  and an option likelihood based on the observed market prices of options, evaluated under the RN measure  $\mathbf{Q}$  using our pricing kernel.

The conditional return density under  $\mathbf{P}$  is normal:

$$f(r_t|\mathcal{F}t-1) = \frac{1}{\sqrt{2\pi h_t}} \exp\left(-\frac{(r_t - e_t)^2}{2h_t}\right),$$

where  $e_t$  and  $h_t$  are the conditional mean and variance specified in Section 3.5. The log-likelihood for returns is:

$$\log L_R \propto -\frac{1}{2} \sum_{t=1}^T \left\{ \log h_t + \frac{(r_t - e_t)^2}{h_t} \right\}.$$

For the option likelihood, we define vega-weighted pricing errors for each option  $i$ :

$$\varepsilon_i = \frac{C_i^{\text{Mkt}} - C_i^{\text{Mod}}}{\text{BSV}_i^{\text{Mkt}}},$$

where  $C_i^{\text{Mkt}}$  is the market price,  $C_i^{\text{Mod}}$  is the model-implied price, and  $\text{BSV}_i^{\text{Mkt}}$  is the Black-Scholes vega computed at the market-implied volatility. As discussed by Trolle

and Schwartz (2009), the normalization is very similar in value to the implied volatility but does not need a complex transformation of the model price, which has to be repeatedly calculated in optimization.

Assuming  $\varepsilon_i \sim \mathcal{N}(0, \sigma_\varepsilon^2)$  and concentrating out  $\sigma_\varepsilon^2$  with its sample counterpart  $\hat{\sigma}_\varepsilon^2 = \frac{1}{N} \sum_i \varepsilon_i^2$ , the log-likelihood from option prices becomes:

$$\log L_O \propto -\frac{N}{2} \log \left( \frac{1}{N} \sum_{i=1}^N \varepsilon_i^2 \right).$$

The full parameter set  $\Theta$  includes all parameters governing the physical dynamics, the pricing kernel, and the evolution of time-varying preference parameters. The full joint likelihood is maximized:

$$\hat{\Theta} = \arg \max_{\Theta} \{ \log L_R(\Theta) + \log L_O(\Theta) \}.$$

This joint estimation approach ensures that the inferred parameters rationalize both return dynamics and option prices under a unified pricing kernel. Moreover, it allows for assessing the contribution of DA preferences to option valuation in a statistically disciplined manner.

## Data

To estimate the model, we use data on S&P 500 options from Chicago Mercantile Exchange (CME), covering the period from January 1, 1996, to December 31, 2021. Consistent with previous studies and to ensure computational feasibility, we use option prices from Wednesdays to estimate models based on longer-dated options. For each trading day, we select the six contracts with the highest trading volume for each available maturity. For the one-day-to-maturity option analysis, we use data from all weekdays. Since our analysis is conducted using call prices, we employ put-call parity to convert put prices into equivalent call prices at a given strike. To estimate the parameters of the physical return dynamics, we use the S&P 500 index level from the CME dataset. Summary statistics for the options and return data are reported in Table 2.

Table 2 panel (a) shows the high annualized return for our sample period 2000 and 2010s. Furthermore, we also see that the typical negative skew that we observe in the returns for the S&P 500 is present in our sample period. Panel (b) shows the descriptive statistics by  $\tau$  and panel (c) by moneyness. The contracts are relatively evenly distributed over  $\tau$ . The distribution of contracts over the strike is tilted slightly towards the out of the money call options with  $M > 1.06$ .

## 5 Results

We divide our empirical investigation into two part: the pricing of one-day options and the pricing of options with maturity higher than one day.

Table 2: Returns and option data

Mean	Standard deviation	Skewness	Kurtosis
0.114	0.233	-0.413	13.499

(a) SPX return statistics

	$\tau \leq 30$	$30 < \tau \leq 60$	$60 < \tau \leq 90$	$90 < \tau \leq 120$	$120 < \tau \leq 180$	$\tau > 180$	All
# of Contracts	15636	19068	11604	8388	13428	0	71136
Average IV %	20.88	21.51	22.74	23.21	22.82		22.11
Average price	155.35	173.43	196.33	252.67	288.76		208.04
Average Vega	139.20	169.21	213.21	266.05	338.01		213.07

(b) Option statistics by maturity

	$M \leq 0.96$	$0.96 < M \leq 0.98$	$0.98 < M \leq 1.02$	$1.02 < M \leq 1.04$	$1.04 < M \leq 1.06$	$M > 1.06$	All
# of Contracts	10437	5698	15326	5947	5335	28393	71136
Average IV %	16.28	13.57	15.31	17.76	19.50	31.04	22.11
Average price	12.22	20.93	48.07	90.49	126.17	443.92	208.04
Average Vega	186.90	257.54	306.94	263.05	238.86	147.78	213.07

(c) Option statistics by moneyness

This table presents summary statistics for the dataset used in the analysis. Panel (a) reports the mean, standard deviation, skewness, and kurtosis of the log return distribution. Panel (b) provides option-level statistics across moneyness buckets, including the number of contracts, average implied volatility, average option price, and average Black-Scholes vega. Panel (c) presents the same set of statistics, but grouped by maturity.

Table 3: Available options

	$M \leq 0.96$	$0.96 < M \leq 0.98$	$0.98 < M \leq 1.02$	$1.02 < M \leq 1.04$	$1.04 < M \leq 1.06$	$M > 1.06$
$\tau \leq 30$	666	1555	4955	1780	1420	2238
$30 < \tau \leq 60$	2055	1713	4245	1745	1644	4518
$60 < \tau \leq 90$	1773	770	2451	849	745	3322
$90 < \tau \leq 120$	1415	500	1348	542	510	2490
$120 < \tau \leq 180$	2778	736	1669	734	698	4269

This table reports the number of option contracts used in the estimation, categorized by time-to-maturity and moneyness. The sample period spans from January 1, 1996, to December 31, 2021.

## 5.1 One-day options: Isolating disappointment aversion

To measure disappointment aversion in its purest form, we analyze one-day options. These ultra-short maturities allow us to sidestep assumptions about the dynamics of the physical and risk-neutral processes over time. Moreover, Equation (15) provides a direct evaluation of the option price. This enabling direct estimation of the pricing kernel parameters from cross-sectional data, provided a sufficient number of strikes are available for a given day. We compare two specifications: a baseline model without DA ( $\gamma_{3t} = 0$ ), following Christoffersen et al. (2013), and the model that includes the DA component. Figure 8 presents the resulting time series of parameter estimates, alongside the pricing errors for the no-DA and DA model.

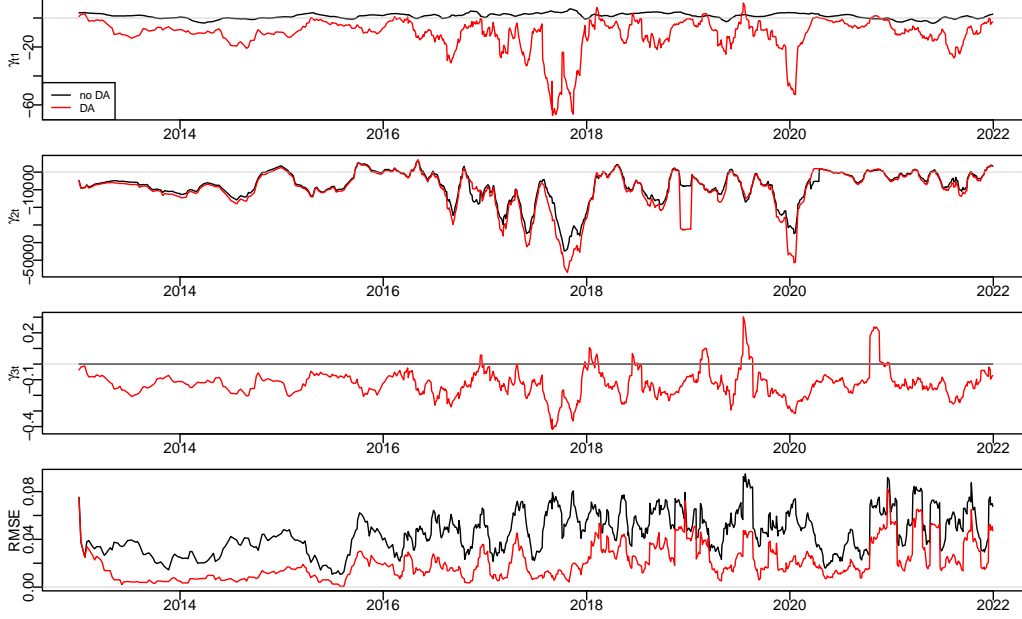
The first three panels display the estimated values of  $\gamma_{1t}$ ,  $\gamma_{2t}$ , and  $\gamma_{3t}$ . The DA model exhibits greater volatility in  $\gamma_{1t}$ , including some large negative realizations.  $\gamma_{2t}$  is mainly negative and comparable across models. Interestingly, the estimated  $\gamma_{3t}$  values are mostly negative, with occasional sharp positive spikes. Negative  $\gamma_{3t}$  implies that, rather than exhibiting DA, the left side of the RN distribution receives less weight, effectively capturing a preference for positive outcomes. This pattern is consistent with empirical findings by Bryzgalova et al. (2023), who document that retail investors, responsible for around 60% of option trading volume, primarily trade short-dated, at-the-money call options. These findings align with negative values of  $\gamma_{3t}$  and support the view that, rather than addi-



tionally penalizing negative returns, market prices exhibit a skew toward gain-seeking on the right side of the distribution.

The fourth panel shows the pricing errors, measured as  $(C_i^{\text{Mkt}} - C_i^{\text{Mod}})/C_i^{\text{Mkt}}$ . Across most days, the DA model yields lower errors than the no-DA benchmark. These findings underscore the empirical value of incorporating DA, or its inverse, in shaping the RN distribution, even at the shortest horizons.

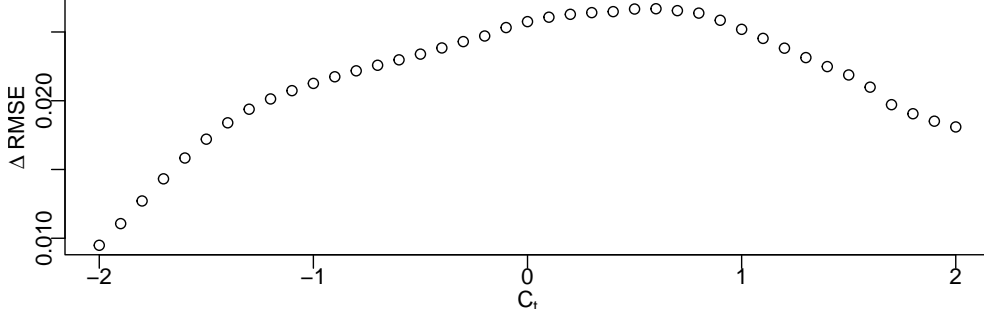
Figure 8: Estimates for one-day options



These figures display the daily estimates of  $\gamma_{1t}$ ,  $\gamma_{2t}$ , and  $\gamma_{3t}$ , obtained from one-day option data using Equation (15). Parameters are estimated separately under the no-DA and DA specifications. The first three panels present the time series of  $\gamma_{1t}$ ,  $\gamma_{2t}$ , and  $\gamma_{3t}$ , respectively. The fourth panel plots the root mean squared pricing error, calculated from  $(C_i^{\text{Mkt}} - C_i^{\text{Mod}})/C_i^{\text{Mkt}}$ , over time. In each panel, the black line corresponds to the no-DA model, while the red line reflects estimates under the DA specification.

Figure 9 displays the difference in mean RMSE between the DA model and the no-DA benchmark across a range of  $C_t$  values from  $-2$  to  $2$ . The resulting curve exhibits an inverse U-shape, with the largest reduction in pricing error occurring when  $C_t$  is near zero. This suggests that the improvement in fit provided by DA is most pronounced when the threshold for disappointment closely aligns with the center of the return distribution. At more extreme values of  $C_t$ , either deep in the left or right tail, the DA model offers less additional explanatory power over the benchmark. The result reinforces the interpretation that disappointment aversion is most powerful when the reference point for disappointment lies close to the current level, supporting the canonical assumption that losses are evaluated relative to a zero or slightly positive return.

Figure 9: One-day options: DA threshold versus fit



This figure shows the difference in the mean RMSE between the no-DA and DA models as a function of the DA threshold  $C_t$ . The RMSE is computed as  $(C_i^{\text{Mkt}} - C_i^{\text{Mod}})/C_i^{\text{Mkt}}$ , and then averaged across all dates.

## 5.2 Parameter estimates for longer horizons options

We now turn our attention to the valuation of option contracts with maturity higher than one day. As discussed, contrary to the one day option, pricing multi-horizon option requires the specification and the estimation of the parameters governing the laws of motion of the physical dynamic and pricing kernel.

Table 4 presents the parameter estimates for the physical process. The estimates for  $\lambda$ ,  $\beta_0$ ,  $\beta_1$ ,  $\beta_2$ , and  $\theta$  are broadly in line with those reported in [Christoffersen et al. \(2013\)](#). The parameter  $\theta$  captures a pronounced leverage effect in the physical process. Notably, the parameter  $\beta_1$ , which governs volatility persistence, is higher than in the more restricted specifications, indicating that shocks to volatility decay more slowly under the physical measure. The included cyclical component in the mean return,  $\tilde{e}_t$ , is estimated to be highly persistent. This richer structure of the physical process provides a solid foundation for analyzing the additional preference-based distortions introduced in the RN measure.

Table 4: Parameter estimates physical process

	$\lambda$	$\alpha_0$	$\alpha_1$	$\alpha_2$	$\beta_0$	$\beta_1$	$\beta_2$	$\theta_0$
CHJ	2.40	$-4.90e-5$	0.97	0.06	$2.90e-19$	0.55	$7.90e-7$	750.49
no DA	2.40	$-1.80e-5$	1.00	0.02	$1.00e-18$	0.79	$2.70e-6$	262.61
DA	2.40	$-1.30e-5$	0.99	0.02	$3.40e-21$	0.97	$2.90e-6$	63.86

This table reports the parameter estimates for the physical process. The specification of the physical dynamics is described in Section 3.5.

We now turn our attention to the estimation of the pricing kernel dynamic. Table 5 reports the parameter estimates of the pricing kernel as well as the overall option pricing error. Several conclusions can be drawn, firstly in the absence of DA, enriching the dynamic of  $\gamma_{2t}$  decreases the VWRMSE only slightly. Indeed, the VWRMSE for the CHJ model is 5.12 whereas that of no DA is 5.06, suggesting limited overall gains in fit. Second, Table 6 shows that this modest improvement masks more nuanced effects: the no-DA pricing kernel improves accuracy for longer-dated contracts but does so at the cost of worse pricing for short-dated options with low moneyness. Part of the improvement in the longer-dated options is linked to the introduction of richer dynamics for  $\gamma_{2t}$ , which provides greater flexibility in accommodating non-trivial term structures in risk premia.

Notably, long-dated high moneyness options continue to exhibit the largest pricing errors.

Table 5: Parameter estimates Pricing Kernel

	$\bar{\alpha}_0$	$\bar{\alpha}_1$	$\bar{\alpha}_2$	$\beta_0$	$\beta_1$	$\beta_2$	$\theta$	VWRMSE
CHJ							773.28	5.12
no DA				$3.80e-20$	0.70	$1.60e-6$	425.35	5.06
DA	$8.90e-7$	0.99	0.00e0	$2.00e-18$	0.65	$1.70e-6$	439.75	4.05

This table reports the parameter estimates for the different versions of the pricing kernel. The first row presents the estimates for the most restrictive specification, following CHJ. The second row reports the results for the no-DA model, where the dynamics for  $\bar{h}_t$  are governed by Equation (17). The third row shows the estimates for the DA model. The final column reports the Black-Scholes VWRMSE.

Despite leaving the common parameters effectively unchanged, the introduction of the DA component in the most flexible specification yields a substantial improvement in fit, lowering the VWRMSE to 4.05. This gain is largely attributable to the added flexibility of the pricing kernel to accommodate left-side sensitivity. The estimated parameters  $\bar{\alpha}_0$ ,  $\bar{\alpha}_1$ , and  $\bar{\alpha}_2$  indicate that the DA distortion is persistent and evolves smoothly over time.

### 5.3 Dissecting the pricing errors

Table 6 illustrates how this improvement translates into more accurate pricing across the volatility surface. Using the CHJ specification as a baseline, the DA model achieves lower pricing errors across most of the volatility surface. These improvements are particularly evident for long-dated, high-moneyness contracts. However, the DA model sacrifices some accuracy for short-dated options with moneyness  $M \leq 0.98$ , where pricing errors increase modestly compared to the baseline. These results underscore the empirical relevance of DA in shaping the RN distribution, particularly by allowing for asymmetry between the left and right sides of the distribution.

Figure 10 illustrates the evolution of pricing errors over time, highlighting the impact of relaxing restrictions on the dynamics of the price of risk. There is substantial variation in pricing error across all models, with the DA model consistently outperforming the more restrictive specifications. The improvement from incorporating DA is particularly pronounced during calmer periods between crises, aligning with the findings of Schreindorfer and Sichert (2025), who show that risk sensitivities tend to be higher during low-volatility environments. In these intervals, the DA model offers the flexibility needed to better capture pricing differences between low- and high-moneyness options. Notably, the largest pricing errors often occur when the VIX has declined sharply but the estimated physical volatility remains elevated due to its persistence.

### 5.4 Model implied pricing kernel parameters

Figure 11 shows the time series of the risk sensitivity parameters  $\gamma_{1t}$ ,  $\gamma_{2t}$ , and  $\gamma_{3t}$  for the three different model specifications. The top panel displays the evolution of  $\gamma_{1t}$ , which appears highly volatile under the CHJ model. In contrast, the DA specification produces a much more stable path for  $\gamma_{1t}$ , with values oscillating around one, reflecting a more consistent level of sensitivity to the linear price of risk. The center panel shows the dynamics of  $\gamma_{2t}$ , where variation is relatively muted under the CHJ but becomes far

Table 6: VWRMSE by Vol surface region

	$M \leq 0.96$	$0.96 < M \leq 0.98$	$0.98 < M \leq 1.02$	$1.02 < M \leq 1.04$	$1.04 < M \leq 1.06$	$M > 1.06$
$\tau \leq 30$	4.91	3.48	3.06	2.94	3.58	5.48
$30 < \tau \leq 60$	3.33	2.95	2.95	2.82	3.09	5.57
$60 < \tau \leq 90$	2.86	2.68	2.83	3.24	3.17	6.72
$90 < \tau \leq 120$	2.99	2.70	2.95	3.15	3.33	8.96
$120 < \tau \leq 180$	2.83	2.70	2.90	3.05	3.36	9.26

(a) CHJ version

	$M \leq 0.96$	$0.96 < M \leq 0.98$	$0.98 < M \leq 1.02$	$1.02 < M \leq 1.04$	$1.04 < M \leq 1.06$	$M > 1.06$
$\tau \leq 30$	5.91	4.62	3.46	3.01	3.49	5.16
$30 < \tau \leq 60$	3.86	3.34	2.94	2.68	2.92	5.41
$60 < \tau \leq 90$	2.76	2.47	2.47	2.69	2.75	6.64
$90 < \tau \leq 120$	2.72	2.50	2.56	2.69	2.99	8.82
$120 < \tau \leq 180$	2.59	2.22	2.51	2.47	2.91	9.13

(b) no DA version

	$M \leq 0.96$	$0.96 < M \leq 0.98$	$0.98 < M \leq 1.02$	$1.02 < M \leq 1.04$	$1.04 < M \leq 1.06$	$M > 1.06$
$\tau \leq 30$	5.96	4.66	3.37	2.79	3.19	4.74
$30 < \tau \leq 60$	4.09	3.34	2.85	2.48	2.65	4.23
$60 < \tau \leq 90$	3.07	2.45	2.35	2.55	2.61	4.42
$90 < \tau \leq 120$	2.90	2.43	2.50	2.65	2.93	5.65
$120 < \tau \leq 180$	2.65	2.10	2.40	2.46	2.99	6.83

(c) DA version where  $C_t = -0$ 

This table reports the VWMSE for options falling within specific maturity and moneyness ranges. Panels (a), (b), and (c) present the results for the CHJ model, the no-DA model, and the DA model, respectively.

more pronounced in the no-DA and DA version. This heightened variation is particularly evident during episodes where market-implied volatility rises moderately from previously low levels. The bottom panel shows that  $\gamma_{3t}$ , which governs DA, tends to increase in these same periods, amplifying the effect by widening and reshaping the RN distribution. The interaction between  $\gamma_{2t}$  and  $\gamma_{3t}$  appears especially impactful in reducing pricing errors during calm periods between crises ([Schreindorfer and Sichert 2025](#)).

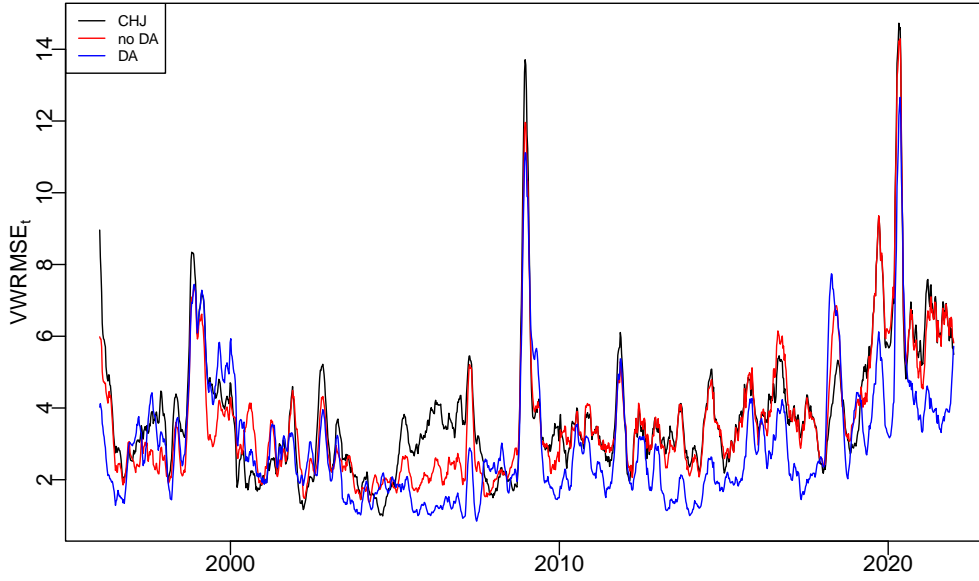
## 5.5 Model implied risk-neutral moments

Figure 12 presents the evolution of the one-period-ahead RN moments across the three model specifications. The RN mean is frequently negative, particularly under the DA specification. As discussed earlier in the context of  $C_t = 0$ , this pattern reflects episodes where  $\gamma_{3t} > 0$ , shifting mass toward the left tail and lowering the mean. However, similar patterns are also observed under the no-DA and CHJ specifications, indicating that part of the negative first moment arises independently of the DA component.

The second panel shows that both the no-DA and DA models capture greater time variation in the RN variance compared to the CHJ specification. This is especially evident during periods when the CHJ model also reports elevated second moments. This suggests that the richer volatility dynamics in the extended models help better track changes in perceived market uncertainty.

The third panel reports the time series of skewness. When  $C_t = 0$ , a positive value of  $\gamma_{3t}$  is associated with positive skewness, as shown analytically in Section 3.2. The small magnitude of the realized one-period-ahead skewness is due to the simultaneous effect of  $\gamma_{3t}$  on both the first and third moments. Finally, the fourth panel shows that excess kurtosis remains relatively stable over time and low in level, but its fluctuations exhibit some correlation with the skewness series. This suggests that changes in asymmetry in the RN distribution are often accompanied by subtle shifts in tail thickness.

Figure 10: Daily VWRMSE for the three different pricing kernels.



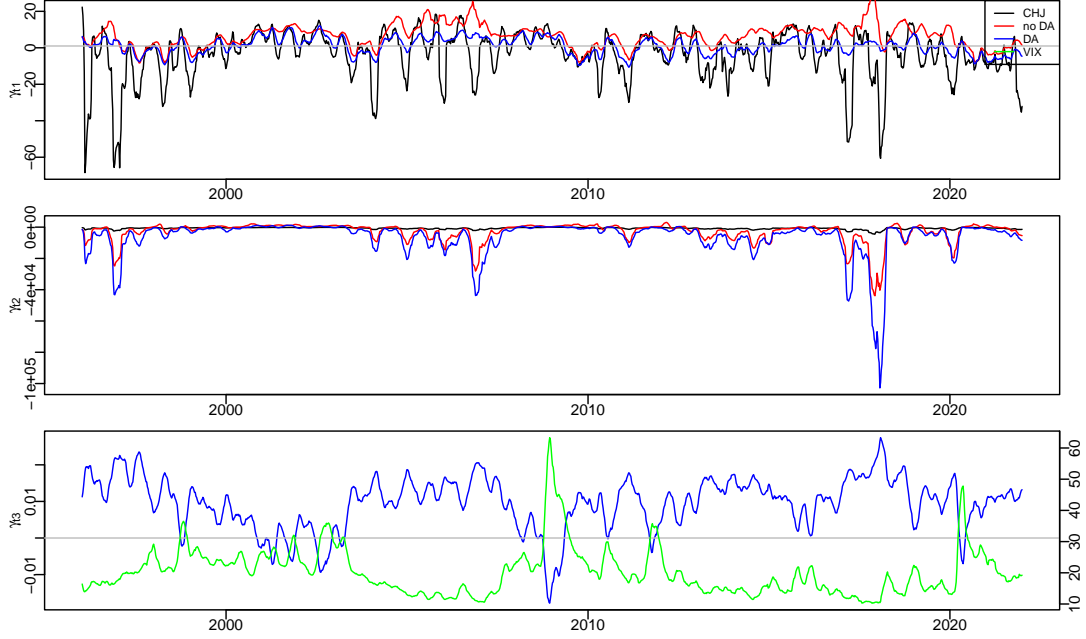
This figure shows the 10-period moving average of the Wednesdays' VWRMSE for the three different version of the model. The black line presents the daily pricing errors for CHJ pricing kernel. The red line presents the VWRMSE no DA of the model and the blue line shows the daily VWRMSE for the DA model.

Figure 13 displays the term structure of the RN second moment across the three model specifications. The CHJ specification generates a distinctly upward-sloping term structure of annualized RN variance, particularly at longer maturities. The no-DA model departs from this pattern: while its overall variance level exhibits greater temporal variation, it still produces a relatively steep term structure. The DA model yields a term structure of RN variance that closely resembles that of the no-DA model but with more pronounced peaks in RN volatility. Moreover, its term structure appears somewhat flatter than that of the no-DA model. On average, the spread between 90- and 180-day annualized volatility is approximately 1.5 volatility points lower under the DA model, more in line with the findings of [Dew-Becker et al. \(2017\)](#). They find that the majority of the variance risk premium is concentrated at the short end of the term structure.

Figure 14 displays the term structure of RN skewness for the three model specifications. The CHJ model, shown in the top panel, exhibits relatively little variation in skewness across maturities, particularly at longer horizons. In contrast, the no-DA model allows for richer dynamics in the sensitivity to risk through time-varying  $\gamma_{1t}$  and  $\gamma_{2t}$ . This added flexibility introduces meaningful variation in the term structure of skewness, as shown in the middle panel. This added flexibility translates into improved pricing performance, especially for longer-dated options where asymmetries in the RN distribution seems to become more relevant.

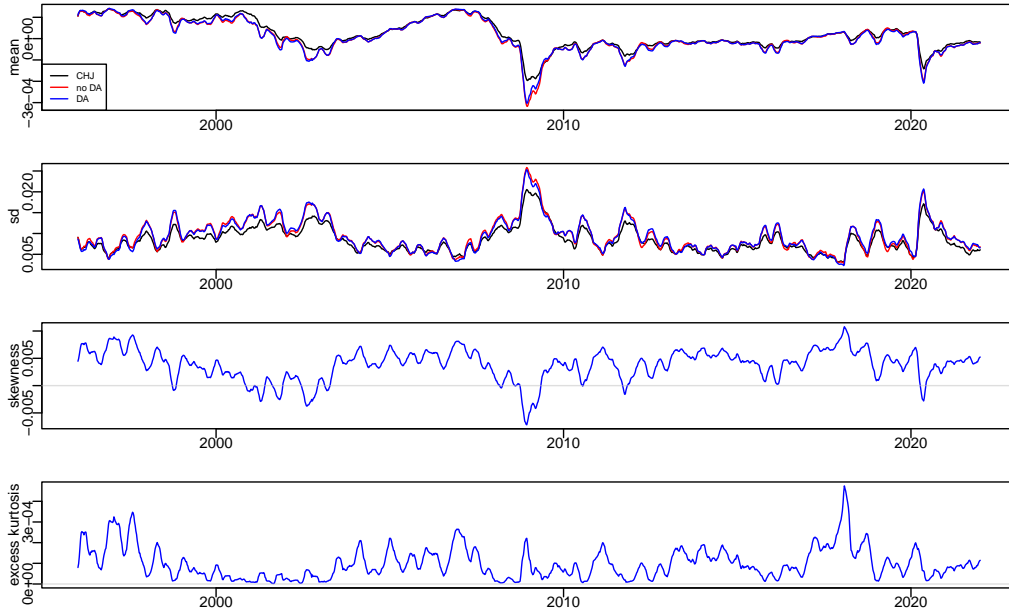
Although the skewness for one-period-ahead in the DA model appears relatively flat, as seen in Figure 12, the DA specification still produces a more pronounced variation in skewness at longer maturities than either of the more restricted alternatives. This is evident in the bottom panel, where the sensitivity of the DA model to DA enables it to capture subtle shifts in asymmetry over time.

Figure 11:  $\gamma_{1t}$ ,  $\gamma_{2t}$  and  $\gamma_{3t}$  for the 3 different versions of the model.



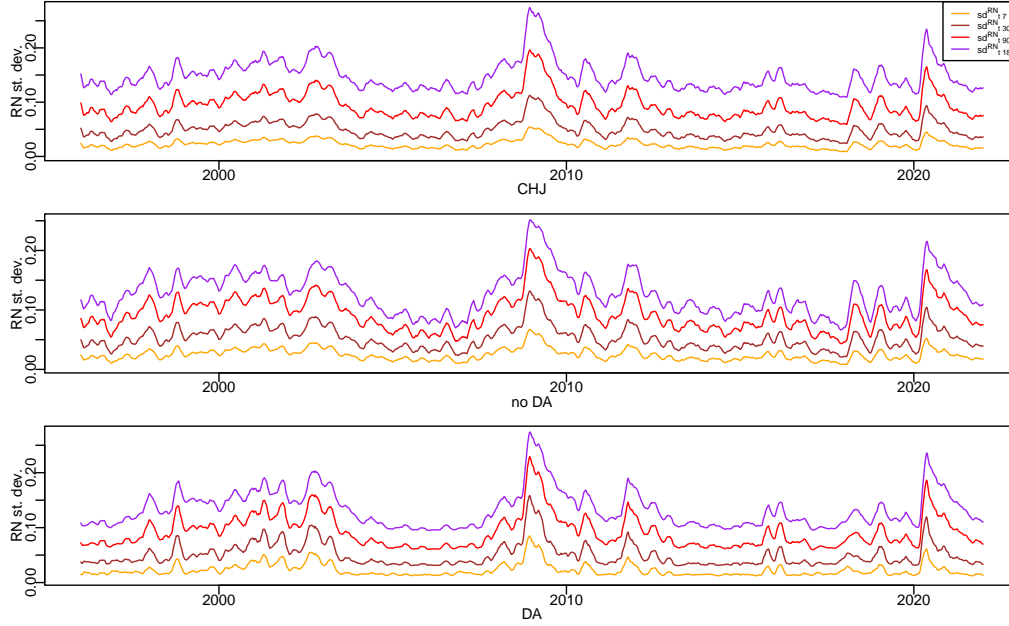
These figures depict the estimates of  $\gamma_{1t}$ ,  $\gamma_{2t}$ , and  $\gamma_{3t}$  extracted under three different versions of the pricing kernel. Panels (a), (b), and (c) present the estimates for  $\gamma_{1t}$ ,  $\gamma_{2t}$ , and  $\gamma_{3t}$ , respectively. The black line corresponds to the CHJ model, the red line to the flexible no-DA model, and the blue line to the DA model. In Panel (c), the green line displays the VIX index for comparison. All series are shown as 10-period moving averages.

Figure 12: One day ahead RN moments



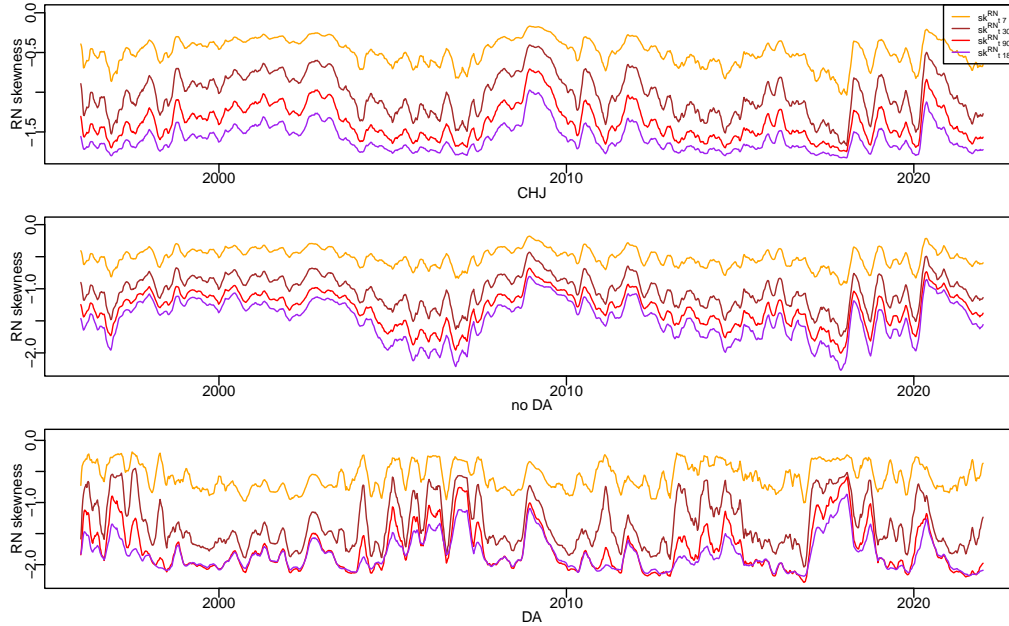
These figures display the one-day-ahead RN moments implied by the three different models. The moments are computed using the optimized parameter estimates, with the DA model evaluated at  $C_t = 0$ .

Figure 13: Risk neutral volatility



These figures depict the estimated RN volatility across different maturities. The square root of the second moments are shown for 1-, 30-, 90-, and 180-day horizons. Each panel corresponds to one of the three versions of the pricing kernel. For readability, the figures present 10-period moving averages of the estimated volatility. The lines are expressed in annualized volatility.

Figure 14: risk neutral skewness



These figures depict the estimated RN skewness across different maturities. The skewness is shown for 1-, 30-, 90-, and 180-day horizons. Each panel corresponds to one of the three versions of the pricing kernel. For readability, the figures present 10-period moving averages of the estimated skewness.



## 5.6 Robustness to EGARCH physical dynamics

To demonstrate the flexibility of the proposed framework, we replace the [Heston and Nandi \(2000\)](#) dynamics with an EGARCH specification for the physical return process. Table 7 reports parameter estimates and pricing errors across the three nested pricing kernel models. The EGARCH parameters governing volatility persistence and asymmetry remain stable across specifications, indicating that the inclusion of DA primarily affects the risk-neutral transformation rather than the physical dynamics themselves in the joint estimation.

The pricing results broadly echo those found under the Heston–Nandi model. The benchmark CHJ model yields a VWRMSE of 7.08. Allowing for richer variance dynamics through a flexible  $\bar{h}_t$  process (no-DA) modestly improves fit, reducing the VWRMSE to 6.57. However, it is the introduction of disappointment aversion that delivers the most substantial improvement: the DA model achieves a VWRMSE of 5.26, a reduction of about 25%. The reduction in pricing error is largest when the DA threshold is set at  $C_t = 0$ , where the pricing kernel distinguishes between gains and losses.

These results reinforce the conclusion that disappointment aversion plays an essential role in shaping investors’ preferences. While the framework accommodates a range of GARCH-type physical processes, it is the DA component that drives the improved pricing performance.

Table 7: Parameter estimates: EGARCH dynamics

	$\lambda$	$\alpha_0$	$\alpha_1$	$\alpha_2$	$\beta_0$	$\beta_1$	$\beta_2$	$\theta_0$
CHJ	0.17	$2.60e-4$	$2.40e-8$	-0.01	-0.22	0.98	0.12	-0.12
no DA	0.17	$2.60e-4$	$7.50e-49$	0.22	-0.36	0.96	0.32	-0.23
DA	0.17	$2.60e-4$	$5.00e-14$	-0.02	-0.37	0.96	0.16	-0.17

(a) Parameters physical process

	$\bar{\alpha}_0$	$\bar{\alpha}_1$	$\bar{\alpha}_2$	$\beta_0$	$\beta_1$	$\beta_2$	$\theta$	VWRMSE
CHJ							-0.12	7.08
no DA				-0.27	0.97	0.25	-0.17	6.57
DA	$8.70e-4$	0.91	0.00e0	-0.27	0.97	0.15	-0.15	5.26

(b) parameters risk neutral process

This table reports the parameter estimates for both the physical process and the risk-neutral pricing kernel. Panel (a) presents the estimates for the physical dynamics, which follow the EGARCH specification. Panel (b) reports the parameter estimates for three versions of the pricing kernel. The first row corresponds to the most restrictive specification, following CHJ. The second row shows estimates for the no-DA model, which incorporates richer dynamics for  $\gamma_{2t}$ . The third row reports the estimates for the full DA model. The final column in Panel (b) presents the Black-Scholes VWRMSE for each specification.

## 6 Conclusion

This paper develops a reduced-form option pricing framework that incorporates disappointment aversion (DA) into a dynamic stochastic discount factor. Building on [Christoffersen et al. \(2013\)](#), our model introduces time-varying sensitivities to return, volatility, and DA, while retaining tractability through a closed-form solution for one-day options. This allows us to cleanly identify investor preference distortions from cross-sectional option prices. Empirically, we estimate three nested models and show that incorporating DA significantly improves pricing accuracy, especially for deep out-of-the-money and medium-term contracts. The DA-enhanced model reduces the vega-weighted root mean squared error by about 20% compared to standard benchmarks. We also uncover rich time variation and horizon-dependence in DA: retail-driven one-day options show gain-seeking behavior, whereas medium-term options reveal traditional disappointment aversion.

While much of the option pricing literature focuses on enriching the physical process, introducing jumps, stochastic volatility, or other features to better match observed prices, our approach shifts the emphasis toward understanding investor preferences given the underlying return dynamics. By embedding disappointment aversion directly into the pricing kernel, we highlight the importance of preference distortions in shaping risk-neutral distributions. This perspective complements structural models and offers a flexible empirical tool to uncover how investors evaluate different market outcomes. In doing so, our framework opens a pathway to better capture the behavioral components embedded in option prices

## References

- Adams, G., J.-S. Fontaine, and C. Ornathanalai (2024). “The market for 0-days-to-expiration: The role of liquidity providers in volatility attenuation”. In: *Available at SSRN*.
- Ang, A., G. Bekaert, and J. Liu (2005). “Why stocks may disappoint”. In: *Journal of financial economics* 76.3, pp. 471–508.
- Ang, A., J. Chen, and Y. Xing (2006). “Downside risk”. In: *The review of financial studies* 19.4, pp. 1191–1239.
- Babaoglu, K., P. Christoffersen, S. Heston, and K. Jacobs (2018). “Option valuation with volatility components, fat tails, and nonmonotonic pricing kernels”. In: *The review of asset pricing studies* 8.2, pp. 183–231.
- Babiarz, M. (2024). “Generalized disappointment aversion and the variance term structure”. In: *Journal of financial and quantitative analysis* 59.4, pp. 1796–1820.
- Bates, D. and R. Craine (1999). “Valuing the futures market clearinghouse’s default exposure during the 1987 crash”. In: *Journal of money, credit and banking* 31.2, pp. 248–272.
- Bégin, J.-F., C. Dorion, and G. Gauthier (2020). “Idiosyncratic jump risk matters: Evidence from equity returns and options”. In: *The review of financial studies* 33.1, pp. 155–211.
- Black, F. and M. Scholes (1973). “The pricing of options and corporate liabilities”. In: *Journal of political economy* 81.3, pp. 637–654.
- Bollerslev, T. (1986). “Generalized autoregressive conditional heteroskedasticity”. In: *Journal of econometrics* 31.3, pp. 307–327.
- Bonomo, M., R. Garcia, N. Meddahi, and R. Tedongap (2011). “Generalized disappointment aversion, long-run volatility risk, and asset prices”. In: *Review of financial studies* 24.1, pp. 82–122.
- Breeden, D. T. and R. H. Litzenberger (1978). “Prices of state-contingent claims implicit in option prices”. In: *Journal of business*, pp. 621–651.
- Bryzgalova, S., A. Pavlova, and T. Sikorskaya (2023). “Retail trading in options and the rise of the big three wholesalers”. In: *The journal of finance* 78.6, pp. 3465–3514.
- Calvet, L. E. and A. J. Fisher (2007). “Multifrequency news and stock returns”. In: *Journal of financial economics* 86.1, pp. 178–212.
- Chorro, C. and R. H. Fanirisoa Zazaravaka (2022). “Discriminating between GARCH models for option pricing by their ability to compute accurate VIX measures”. In: *Journal of financial econometrics* 20.5, pp. 902–941.
- Christoffersen, P., R. Elkamhi, B. Feunou, and K. Jacobs (2010). “Option valuation with conditional heteroskedasticity and nonnormality”. In: *The review of financial studies* 23.5, pp. 2139–2183.
- Christoffersen, P., S. Heston, and K. Jacobs (2006). “Option valuation with conditional skewness”. In: *Journal of econometrics* 131.1-2, pp. 253–284.
- Christoffersen, P., S. Heston, and K. Jacobs (2013). “Capturing option anomalies with a variance-dependent pricing kernel”. In: *Review of financial studies* 26.8, pp. 1963–2006.
- Christoffersen, P. and K. Jacobs (2004). “Which GARCH model for option valuation?” In: *Management science* 50.9, pp. 1204–1221.
- Dew-Becker, I., S. Giglio, A. Le, and M. Rodriguez (2017). “The price of variance risk”. In: *Journal of financial economics* 123.2, pp. 225–250.

- Duffee, G. R. (1995). “Term structure of interest rates in a general equilibrium model”. In: *Journal of finance* 50.4, pp. 1277–1302.
- Duffie, D., J. Pan, and K. Singleton (2000). “Transform analysis and asset pricing for affine jump-diffusions”. In: *Econometrica* 68.6, pp. 1343–1376.
- Engle, R. and V. Ng (1993). “Measuring and testing the impact of news on volatility”. In: *Journal of finance* 48.5, pp. 1749–1778.
- Feunou, B., M. R. Jahan-Parvar, and R. Tédongap (2013). “Modeling market downside volatility”. In: *Review of finance* 17.1, pp. 443–481.
- Gul, F. (1991). “A theory of disappointment aversion”. In: *Econometrica* 59.3, pp. 667–686.
- Harvey, C. R. and A. Siddique (2000). “Conditional skewness in asset pricing tests”. In: *Journal of finance* 55.3, pp. 1263–1295.
- Heston, S. L. and S. Nandi (2000). “A closed-form GARCH option valuation model”. In: *The review of financial studies* 13.3, pp. 585–625.
- Kimball, M. S. (1990). “Precautionary saving in the small and in the large”. In: *Econometrica* 58.1, pp. 53–73.
- Maheu, J. M. and T. H. McCurdy (2004). “News arrival, jump dynamics, and volatility components for individual stock returns”. In: *The journal of finance* 59.2, pp. 755–793.
- Majewski, A. A., G. Bormetti, and F. Corsi (2015). “Smile from the past: A general option pricing framework with multiple volatility and leverage components”. In: *Journal of econometrics* 187.2, pp. 521–531.
- Routledge, B. R. and S. E. Zin (2010). “Generalized disappointment aversion and asset prices”. In: *The journal of finance* 65.4, pp. 1303–1332.
- Schreindorfer, D. (2020). “Macroeconomic tail risks and asset prices”. In: *The review of financial studies* 33.8, pp. 3541–3582.
- Schreindorfer, D. and T. Sichert (2025). “Conditional risk and the pricing kernel”. In: *Journal of financial economics* 171, p. 104106.
- Trolle, A. B. and E. S. Schwartz (2009). “Unspanned stochastic volatility and the pricing of commodity derivatives”. In: *The review of financial studies* 22.11, pp. 4423–4461.
- Wu, J. C. and F. D. Xia (2016). “Measuring the macroeconomic impact of monetary policy at the zero lower bound”. In: *Journal of money, credit and banking* 48.2-3, pp. 253–291.

## A Appendix

### A.1 christoffersen2013capturing

$$\begin{aligned}
e_t &= r_f + \lambda h_t - \frac{h_t}{2} \\
h_{t+1} &= \beta_0 + \beta_1 h_t + \beta_2 \left( z_{t+1} - \theta \sqrt{h_t} \right)^2 \\
\tilde{\gamma}_{1,t} &= 0 \longrightarrow \gamma_{3t} = 0 \\
\bar{h}_t &= \psi h_t \longrightarrow \gamma_{2t} = \frac{1 - 1/\psi}{2h_t} \text{ and } \gamma_{1t} = \frac{r_f - \psi e_t}{\psi h_t} - \frac{1}{2}
\end{aligned}$$

### A.2 Detailed derivations

## Physical dynamics

$$\begin{aligned} r_{t+1} &= \ln(S_{t+1}/S_t) \\ r_{t+1} &= e_t + \sqrt{h_t} z_{t+1} \\ z_t &\sim i.i.d.N(0, 1) \end{aligned}$$

Example of dynamics for  $e_t$  and  $h_t$  routinely used in the GARCH-Option pricing literature are:

$$\begin{aligned} e_t &= r_f + \lambda h_t - \frac{h_t}{2} + \tilde{e}_t \\ \tilde{e}_{t+1} &= \alpha_0 + \alpha_1 \tilde{e}_t + \alpha_2 \sqrt{h_t} z_{t+1} \end{aligned}$$

$$h_{t+1} = \beta_0 + \beta_1 h_t + \beta_2 \left( z_{t+1} - \theta \sqrt{h_t} \right)^2$$

The following discussions are not restricted to these dynamics.

## Pricing-Kernel

$$\begin{aligned} \widetilde{PK}_{t+1} &\equiv (1 + \gamma_{3t} 1_{[r_{t+1} < -\kappa_t]}) \times \exp(\gamma_{1t} r_{t+1} + \gamma_{2t} r_{t+1}^2) \\ PK_{t+1} &= \frac{\widetilde{PK}_{t+1}}{E_t[\widetilde{PK}_{t+1}]} \end{aligned}$$

$$E_t[\widetilde{PK}_{t+1}] = E_t[\exp(\gamma_{1t} r_{t+1} + \gamma_{2t} r_{t+1}^2)] + \gamma_{3t} E_t[\exp(\gamma_{1t} r_{t+1} + \gamma_{2t} r_{t+1}^2) 1_{[r_{t+1} < -\kappa_t]}]$$

$$\begin{aligned} &E_t[\exp(\gamma_{1t} r_{t+1} + \gamma_{2t} r_{t+1}^2)] \\ &= E_t\left[\exp\left(\gamma_{1t} \left(e_t + \sqrt{h_t} z_{t+1}\right) + \gamma_{2t} \left(e_t + \sqrt{h_t} z_{t+1}\right)^2\right)\right] \\ &= \exp\left(\gamma_{1t} e_t + \gamma_{2t} e_t^2 - \frac{1}{2} \ln(1 - 2\gamma_{2t} h_t) + \frac{(\gamma_{1t} + 2\gamma_{2t} e_t)^2 h_t}{2(1 - 2\gamma_{2t} h_t)}\right) \\ &= \frac{1}{\sqrt{1 - 2h_t \gamma_{2t}}} \exp\left(\frac{2\gamma_{2t} e_t^2 + 2\gamma_{1t} e_t + h_t \gamma_{1t}^2}{2(1 - 2\gamma_{2t} h_t)}\right) \end{aligned}$$

Manipulating the second part of  $\widetilde{PK}_{t+1}$

$$\begin{aligned} &E_t[\exp(\gamma_{1t} r_{t+1} + \gamma_{2t} r_{t+1}^2) 1_{[r_{t+1} < -\kappa_t]}] \\ &= \int_{-\infty}^{-\kappa_t} \frac{1}{\sqrt{2\pi h_t}} \exp\left(\gamma_{1t} r_{t+1} + \gamma_{2t} r_{t+1}^2 - \frac{(r_{t+1} - e_t)^2}{2h_t}\right) dr_{t+1} \\ &= E_t[\exp(\gamma_{1t} r_{t+1} + \gamma_{2t} r_{t+1}^2)] \Phi\left(\frac{-\kappa_t - \frac{(e_t + h_t \gamma_{1t})}{(1 - 2h_t \gamma_{2t})}}{\sqrt{\frac{h_t}{(1 - 2h_t \gamma_{2t})}}}\right) \end{aligned}$$

Hence it must be the case that

$$1 - 2h_t\gamma_{2t} > 0 \iff \gamma_{2t} < \frac{1}{2h_t}$$

$$\begin{aligned} E_t [\widetilde{PK}_{t+1}] &= E_t [\exp(\gamma_{1t}r_{t+1} + \gamma_{2t}r_{t+1}^2)] + \gamma_{3t}E_t [\exp(\gamma_{1t}r_{t+1} + \gamma_{2t}r_{t+1}^2) 1_{[r_{t+1} < -\kappa_t]}] \\ &= (1 + \gamma_{3t}\Phi(C_t)) E_t [\exp(\gamma_{1t}r_{t+1} + \gamma_{2t}r_{t+1}^2)] \end{aligned}$$

## Risk neutral dynamics

$$\begin{aligned} E_t^Q [\exp(ur_{t+1})] &= E_t [PK_{t+1} \exp(ur_{t+1})] = \frac{E_t [\widetilde{PK}_{t+1} \exp(ur_{t+1})]}{E_t [\widetilde{PK}_{t+1}]} \\ &= \left( \frac{1 + \gamma_{3t}\Phi(C_t(u))}{1 + \gamma_{3t}\Phi(C_t)} \right) \exp\left(a_{1,t}u + \frac{\bar{h}_t}{2}u^2\right) \end{aligned}$$

$$\begin{aligned} C_t &= \frac{-\kappa_t - a_{1,t}}{\sqrt{\bar{h}_t}}; \quad C_t(u) = \frac{-\kappa_t - \frac{(e_t + h_t(\gamma_{1t} + u))}{(1 - 2h_t\gamma_{2t})}}{\sqrt{\frac{h_t}{(1 - 2h_t\gamma_{2t})}}} = C_t - \sqrt{\bar{h}_t}u \\ a_{1,t} &\equiv \frac{\gamma_{1t}h_t + e_t}{1 - 2\gamma_{2t}h_t}; \quad \bar{h}_t \equiv \frac{h_t}{1 - 2h_t\gamma_{2t}} \end{aligned}$$

hence

$$E_t^Q [\exp(ur_{t+1})] = \left( \frac{1 + \gamma_{3t}\Phi(C_t - \sqrt{\bar{h}_t}u)}{1 + \gamma_{3t}\Phi(C_t)} \right) \exp\left(a_{1,t}u + \frac{\bar{h}_t}{2}u^2\right)$$

$$\bar{r}_{t+1} \sim^Q N(a_{1,t}, \bar{h}_t); \gamma_{3t} = 0 \implies r_{t+1} \sim^Q N\left(r_f - \frac{\bar{h}_t}{2}, \bar{h}_t\right)$$

$$\begin{aligned} E_t^Q [\exp(u\bar{r}_{t+1}) 1_{[\bar{r}_{t+1} < -\kappa_t]}] &= \int_{-\infty}^{-\kappa_t} \frac{1}{\sqrt{2\pi\bar{h}_t}} \exp\left(u\bar{r}_{t+1} - \frac{(\bar{r}_{t+1} - a_{1,t})^2}{2\bar{h}_t}\right) d\bar{r}_{t+1} \\ &= \exp\left(a_{1,t}u + \frac{\bar{h}_t}{2}u^2\right) \Phi(C_t - \sqrt{\bar{h}_t}u) \end{aligned}$$

$$\begin{aligned} E_t^Q [\exp(ur_{t+1})] &= \left( \frac{1 + \gamma_{3t}\Phi(C_t - \sqrt{\bar{h}_t}u)}{1 + \gamma_{3t}\Phi(C_t)} \right) \exp\left(a_{1,t}u + \frac{\bar{h}_t}{2}u^2\right) \\ &= \frac{E_t^Q [\exp(u\bar{r}_{t+1})] + \gamma_{3t}E_t^Q [\exp(u\bar{r}_{t+1}) 1_{[\bar{r}_{t+1} < -\kappa_t]}]}{1 + \gamma_{3t}E_t^Q [1_{[\bar{r}_{t+1} < -\kappa_t]}]} \\ &= E_t^Q \left[ \frac{1 + \gamma_{3t}1_{[\bar{r}_{t+1} < -\kappa_t]}}{1 + \gamma_{3t}E_t^Q [1_{[\bar{r}_{t+1} < -\kappa_t]}]} \exp(u\bar{r}_{t+1}) \right] \end{aligned}$$

## First interpretation

Let us denote by  $Q^{nd}$  the No-Disappointment risk-Neutral probability,

$$r_{t+1} \sim^{Q^{nd}} N(a_{1,t}, \bar{h}_t)$$

the pricing kernel which enable us to move from  $Q^{nd}$  to  $Q$  is given by

$$PK_{t+1}^{nd} = \frac{1 + \gamma_{3t} 1_{[r_{t+1} < -\kappa_t]}}{1 + \gamma_{3t} E_t^{Q^{nd}} [1_{[r_{t+1} < -\kappa_t]}]}$$

$$E_t^Q [\exp(ur_{t+1})] = E_t^{Q^{nd}} \left[ \frac{1 + \gamma_{3t} 1_{[r_{t+1} < -\kappa_t]}}{1 + \gamma_{3t} E_t^{Q^{nd}} [1_{[r_{t+1} < -\kappa_t]}]} \exp(ur_{t+1}) \right]$$

## Second interpretation

$$\bar{r}_{t+1} \sim^Q N(a_{1,t}, \bar{h}_t)$$

$$E_t^Q [\exp(u\bar{r}_{t+1}) | -\kappa_t < \bar{r}_{t+1}] = \left( \frac{1 - \Phi(C_t - \sqrt{\bar{h}_t}u)}{1 - \Phi(C_t)} \right) \exp\left(a_{1,t}u + \frac{\bar{h}_t}{2}u^2\right)$$

$$E_t^Q [\exp(u\bar{r}_{t+1}) | \bar{r}_{t+1} \leq -\kappa_t] = \left( \frac{\Phi(C_t - \sqrt{\bar{h}_t}u)}{\Phi(C_t)} \right) \exp\left(a_{1,t}u + \frac{\bar{h}_t}{2}u^2\right)$$

**when**  $\gamma_{3t} > 0$ ,

$$E_t^Q [\exp(ur_{t+1})] = \left( \frac{1 + \gamma_{3t} \Phi(C_t - \sqrt{\bar{h}_t}u)}{1 + \gamma_{3t} \Phi(C_t)} \right) \exp\left(a_{1,t}u + \frac{\bar{h}_t}{2}u^2\right)$$

$$= \rho_t E_t^Q [\exp(ur_{t+1}) | \bar{r}_{t+1} \leq -\kappa_t] + (1 - \rho_t) E_t^Q [\exp(ur_{t+1})]$$

where

$$\rho_t \equiv \frac{\gamma_{3t} \Phi(C_t)}{1 + \gamma_{3t} \Phi(C_t)}$$

**when**  $\gamma_{3t} \leq 0$ ,

$$E_t^Q [\exp(ur_{t+1})] = \left( \frac{1 + \gamma_{3t} \Phi(C_t - \sqrt{\bar{h}_t}u)}{1 + \gamma_{3t} \Phi(C_t)} \right) \exp\left(a_{1,t}u + \frac{\bar{h}_t}{2}u^2\right)$$

$$= \rho_t E_t^Q [\exp(ur_{t+1}) | -\kappa_t < \bar{r}_{t+1}] + (1 - \rho_t) E_t^Q [\exp(ur_{t+1})]$$

where

$$\rho_t \equiv \frac{-\gamma_{3t} (1 - \Phi(C_t))}{1 + \gamma_{3t} \Phi(C_t)}$$

Hence then under  $Q$ ,  $r_{t+1}$  follows a mixture of truncated Gaussian and Gaussian distribution.



## Risk neutral moments

$$\Psi_t^Q(u) = \ln E_t^Q[\exp(ur_{t+1})] = \ln \left( \frac{1 + \gamma_{3t}\Phi(C_t - \sqrt{\bar{h}_t}u)}{1 + \gamma_{3t}\Phi(C_t)} \right) + a_{1,t}u + \frac{\bar{h}_t}{2}u^2$$

Take  $\Upsilon = C_t - \sqrt{\bar{h}_t}u$  and  $B = 1 + \gamma_{3t}\Phi(\Upsilon)$ , it follows that

$$\begin{aligned}\Psi_t^Q(u)' &= -\sqrt{\bar{h}_t}\gamma_{3t}\frac{\phi(\Upsilon)}{B} + a_{1,t} + \bar{h}_t u \\ \Psi_t^Q(u)'' &= -\bar{h}_t\gamma_{3t}\frac{\gamma_{3t}\phi(\Upsilon)^2 - \phi'(\Upsilon)B}{B^2} + \bar{h}_t \\ \Psi_t^Q(u)''' &= \bar{h}_t^{3/2}\gamma_{3t}\left(\frac{-\phi''(\Upsilon)}{B} + \frac{3\gamma_{3t}\phi(\Upsilon)\phi'(\Upsilon)}{B^2} - \frac{2\gamma_{3t}^2\phi(\Upsilon)^3}{B^3}\right) \\ \Psi_t^Q(u)'''' &= \bar{h}_t^2\gamma_{3t}\left(\frac{\phi'''(\Upsilon)B^3 - 4\gamma_{3t}B^2\phi(\Upsilon)\phi''(\Upsilon) - 3\gamma_{3t}\phi'(\Upsilon)^2B^2}{B^4}\right) + \\ &\quad \bar{h}_t^2\gamma_{3t}\left(\frac{12\gamma_{3t}^2B\phi(\Upsilon)^2\phi'(\Upsilon) - 6\gamma_{3t}^3\phi(\Upsilon)^4}{B^4}\right)\end{aligned}$$

$$\Psi_t^Q(0)' - e_t = (\gamma_{1t} + 2\gamma_{2t}e_t)\bar{h}_t - \frac{\gamma_{3t}\phi(C_t)\sqrt{\bar{h}_t}}{1 + \gamma_{3t}\Phi(C_t)}$$

$$\bar{h}_t \equiv \frac{h_t}{1 - 2h_t\gamma_{2t}}$$

$$\begin{aligned}\gamma_{3t} &= \frac{1 - e^{(\gamma_{1t} - \bar{\gamma}_{1t})\bar{h}_t}}{\Phi(C_t - \sqrt{\bar{h}_t})e^{(\gamma_{1t} - \bar{\gamma}_{1t})\bar{h}_t} - \Phi(C_t)} \\ 1 + \gamma_{3t}\Phi(C_t) &= \frac{(\Phi(C_t - \sqrt{\bar{h}_t}) - \Phi(C_t))e^{(\gamma_{1t} - \bar{\gamma}_{1t})\bar{h}_t}}{\Phi(C_t - \sqrt{\bar{h}_t})e^{(\gamma_{1t} - \bar{\gamma}_{1t})\bar{h}_t} - \Phi(C_t)} \\ \frac{\gamma_{3t}\phi(C_t)\sqrt{\bar{h}_t}}{1 + \gamma_{3t}\Phi(C_t)} &= \frac{(e^{-(\gamma_{1t} - \bar{\gamma}_{1t})\bar{h}_t} - 1)\phi(C_t)\sqrt{\bar{h}_t}}{\Phi(C_t - \sqrt{\bar{h}_t}) - \Phi(C_t)}\end{aligned}$$

$$\begin{aligned}\Psi_t^Q(0)' &= r_f - \frac{1}{2}\bar{h}_t + (\gamma_{1t} - \bar{\gamma}_{1t})\bar{h}_t + \frac{(1 - e^{-(\gamma_{1t} - \bar{\gamma}_{1t})\bar{h}_t})\phi(C_t)\sqrt{\bar{h}_t}}{\Phi(C_t - \sqrt{\bar{h}_t}) - \Phi(C_t)} \\ &\approx r_f - \frac{1}{2}\bar{h}_t + \left[1 + \frac{\phi(C_t)\sqrt{\bar{h}_t}}{\Phi(C_t - \sqrt{\bar{h}_t}) - \Phi(C_t)}\right](\gamma_{1t} - \bar{\gamma}_{1t})\bar{h}_t\end{aligned}$$

$$\begin{aligned}
\frac{\Psi_t^Q(0)''}{\bar{h}_t} - 1 &= \frac{\left(e^{-(\gamma_{1t}-\bar{\gamma}_{1t})\bar{h}_t} - 1\right) \phi'(C_t)}{\Phi(C_t - \sqrt{\bar{h}_t}) - \Phi(C_t)} - \left(\frac{\left(e^{-(\gamma_{1t}-\bar{\gamma}_{1t})\bar{h}_t} - 1\right) \phi(C_t)}{\Phi(C_t - \sqrt{\bar{h}_t}) - \Phi(C_t)}\right)^2 \\
&= \frac{\left(1 - e^{-(\gamma_{1t}-\bar{\gamma}_{1t})\bar{h}_t}\right) \phi(C_t)}{\Phi(C_t - \sqrt{\bar{h}_t}) - \Phi(C_t)} \left[C_t - \frac{\left(1 - e^{-(\gamma_{1t}-\bar{\gamma}_{1t})\bar{h}_t}\right) \phi(C_t)}{\Phi(C_t - \sqrt{\bar{h}_t}) - \Phi(C_t)}\right]
\end{aligned}$$

**no-arbitrage condition**

$$\begin{aligned}
E_t^Q[\exp(r_{t+1})] &= \exp(r_f) \iff \left(\frac{1 + \gamma_{3t}\Phi(C_t - \sqrt{\bar{h}_t})}{1 + \gamma_{3t}\Phi(C_t)}\right) \exp\left(a_{1,t} + \frac{\bar{h}_t}{2}\right) = \exp(r_f) \\
&\iff \gamma_{3t} \left(\Phi(C_t - \sqrt{\bar{h}_t}) - \Phi(C_t) \exp\left(r_f - a_{1,t} - \frac{\bar{h}_t}{2}\right)\right) \\
&= \exp\left(r_f - a_{1,t} - \frac{\bar{h}_t}{2}\right) - 1
\end{aligned}$$

$$\begin{aligned}
\gamma_{3t} &= 0 \iff r_f - a_{1,t} - \frac{\bar{h}_t}{2} = 0 \iff \frac{\gamma_{1t}h_t + e_t}{1 - 2\gamma_{2t}h_t} = r_f - \frac{\bar{h}_t}{2} \\
&\iff \gamma_{1t} = \frac{r_f - \frac{e_t}{1 - 2\gamma_{2t}h_t}}{\bar{h}_t} - \frac{1}{2} \equiv \bar{\gamma}_{1t}
\end{aligned}$$

$$\gamma_{3t} = \frac{\exp\left(r_f - a_{1,t} - \frac{\bar{h}_t}{2}\right) - 1}{\Phi(C_t - \sqrt{\bar{h}_t}) - \Phi(C_t) \exp\left(r_f - a_{1,t} - \frac{\bar{h}_t}{2}\right)}$$

**Conditions for  $\gamma_{3t} > -1$**

$$\begin{aligned}
r_f - a_{1,t} - \frac{\bar{h}_t}{2} &= r_f - \left(\gamma_{1t}\bar{h}_t + \frac{e_t}{1 - 2\gamma_{2t}h_t}\right) - \frac{\bar{h}_t}{2} \\
&= (\bar{\gamma}_{1t} - \gamma_{1t})\bar{h}_t
\end{aligned}$$

$$\gamma_{3t} = \frac{1 - e^{(\gamma_{1t}-\bar{\gamma}_{1t})\bar{h}_t}}{\Phi(C_t - \sqrt{\bar{h}_t}) e^{(\gamma_{1t}-\bar{\gamma}_{1t})\bar{h}_t} - \Phi(C_t)}$$

**Case1:**  $e^{(\gamma_{1t}-\bar{\gamma}_{1t})\bar{h}_t} \geq \frac{\Phi(C_t)}{\Phi(C_t - \sqrt{\bar{h}_t})} > 1$

$$\gamma_{3t} > -1 \iff \frac{\Phi(-C_t)}{\Phi(-C_t + \sqrt{\bar{h}_t})} \geq e^{(\gamma_{1t}-\bar{\gamma}_{1t})\bar{h}_t} \geq \frac{\Phi(C_t)}{\Phi(C_t - \sqrt{\bar{h}_t})} > 1$$

impossible, hence, it should be the case that:

$$\begin{aligned}
e^{(\gamma_{1t}-\bar{\gamma}_{1t})\bar{h}_t} &< \frac{\Phi(C_t)}{\Phi(C_t - \sqrt{\bar{h}_t})} \\
\gamma_{3t} &> -1 \iff \frac{1 - e^{(\gamma_{1t}-\bar{\gamma}_{1t})\bar{h}_t}}{\Phi(C_t - \sqrt{\bar{h}_t}) e^{(\gamma_{1t}-\bar{\gamma}_{1t})\bar{h}_t} - \Phi(C_t)} > -1 \\
&\iff \frac{\Phi(-C_t)}{\Phi(-C_t + \sqrt{\bar{h}_t})} < e^{(\gamma_{1t}-\bar{\gamma}_{1t})\bar{h}_t} < \frac{\Phi(C_t)}{\Phi(C_t - \sqrt{\bar{h}_t})} \\
&\iff \hat{\gamma}_{1t}^l < \gamma_{1t} - \bar{\gamma}_{1t} < \hat{\gamma}_{1t}^u
\end{aligned}$$

where

$$\begin{aligned}
\hat{\gamma}_{1t}^l &\equiv \frac{1}{\bar{h}_t} \ln \left( \frac{\Phi(-C_t)}{\Phi(-C_t + \sqrt{\bar{h}_t})} \right); \quad \hat{\gamma}_{1t}^u \equiv \frac{1}{\bar{h}_t} \ln \left( \frac{\Phi(C_t)}{\Phi(C_t - \sqrt{\bar{h}_t})} \right) \\
\gamma_{1t} - \bar{\gamma}_{1t} &= \hat{\gamma}_{1t}^l - \hat{\gamma}_{1t}^l \frac{\hat{\gamma}_{1t}^u - \hat{\gamma}_{1t}^l}{\hat{\gamma}_{1t}^u \exp(-\tilde{\gamma}_{1t}) - \hat{\gamma}_{1t}^l} = \hat{\gamma}_{1t}^l \hat{\gamma}_{1t}^u \left( \frac{\exp(-\tilde{\gamma}_{1t}) - 1}{\hat{\gamma}_{1t}^u \exp(-\tilde{\gamma}_{1t}) - \hat{\gamma}_{1t}^l} \right)
\end{aligned}$$

### A.3 Model implied option prices

The price of a European call option as:

$$C_m(e_t, h_t, \gamma_{1t}, \gamma_{2t}) = e^{-r_f \tau} E_t^Q [\max(S_{t+\tau} - K, 0)]$$

$$E_t^Q [\max(S_{t+\tau} - K, 0)] = E_t \left[ \left( \prod_{j=1}^{\tau} P K_{t+j} \right) \max(S_{t+\tau} - K, 0) \right]$$

**Computing model implied option prices for  $\tau = 1$**

$$\begin{aligned}
C_m(e_t, h_t, \gamma_{1t}, \gamma_{2t}) &= e^{-r_f} E_t^Q [\max(S_{t+1} - K, 0)] = e^{-r_f} E_t^Q [\max(S_t \exp(r_{t+1}) - K, 0)] \\
&= e^{-r_f} E_t^Q \left[ (S_t \exp(r_{t+1}) - K) 1_{[r_{t+1} > \ln(\frac{K}{S_t})]} \right] \\
C_m(e_t, h_t, \gamma_{1t}, \gamma_{2t}) &= E_t^Q \left[ \exp(r_{t+1}) 1_{[r_{t+1} > \ln(\frac{K}{S_t})]} \right] e^{-r_f} S_t - E_t^Q \left[ 1_{[r_{t+1} > \ln(\frac{K}{S_t})]} \right] e^{-r_f} K
\end{aligned}$$

$$E_t^Q \left[ 1_{[r_{t+1} > \ln(\frac{K}{S_t})]} \right] = \frac{E_t^{Q^{nd}} \left[ 1_{[r_{t+1} > \ln(\frac{K}{S_t})]} \right] + \gamma_{3t} E_t^{Q^{nd}} \left[ 1_{[r_{t+1} < -\kappa_t]} 1_{[r_{t+1} > \ln(\frac{K}{S_t})]} \right]}{1 + \gamma_{3t} E_t^{Q^{nd}} \left[ 1_{[r_{t+1} < -\kappa_t]} \right]}$$

where

$$r_{t+1} \sim^{Q^{nd}} N(a_{1,t}, \bar{h}_t); \quad E_t^{Q^{nd}} [1_{[r_{t+1} < -\kappa_t]}] = \Phi(C_t); \quad C_t = \frac{-\kappa_t - a_{1,t}}{\sqrt{\bar{h}_t}}.$$

Hence

$$E_t^{Q^{nd}} \left[ 1_{[r_{t+1} > \ln(\frac{K}{S_t})]} \right] = 1 - \Phi \left( \frac{\ln(\frac{K}{S_t}) - a_{1,t}}{\sqrt{\bar{h}_t}} \right) = \Phi \left( \frac{a_{1,t} - \ln(\frac{K}{S_t})}{\sqrt{\bar{h}_t}} \right)$$

For ease of presentation  $m_t = \frac{\ln(\frac{K}{S_t}) - a_{1,t}}{\sqrt{\bar{h}_t}}$

$$\begin{aligned} E_t^{Q^{nd}} \left[ 1_{[r_{t+1} < -\kappa_t]} 1_{[r_{t+1} > \ln(\frac{K}{S_t})]} \right] &= 1_{[\ln(\frac{K}{S_t}) < -\kappa_t]} E_t^{Q^{nd}} \left[ 1_{[\ln(\frac{K}{S_t}) < r_{t+1} < -\kappa_t]} \right] \\ &= 1_{[\ln(\frac{K}{S_t}) < -\kappa_t]} \{ \Phi(C_t) - \Phi(m_t) \} \end{aligned}$$

$$\begin{aligned} &E_t^Q \left[ 1_{[r_{t+1} > \ln(\frac{K}{S_t})]} \right] \\ &= \frac{1 - \Phi(m_t) + \gamma_{3t} \{ \Phi(C_t) - \Phi(m_t) \} 1_{[\ln(\frac{K}{S_t}) < -\kappa_t]}}{1 + \gamma_{3t} \Phi(C_t)} \\ &= \left\{ 1 - \frac{(1 + \gamma_{3t}) \Phi(m_t)}{1 + \gamma_{3t} \Phi(C_t)} \right\} 1_{[\ln(\frac{K}{S_t}) < -\kappa_t]} + \frac{1 - \Phi(m_t)}{1 + \gamma_{3t} \Phi(C_t)} 1_{[\ln(\frac{K}{S_t}) \geq -\kappa_t]} \end{aligned}$$

$$\begin{aligned} &E_t^Q \left[ e^{r_{t+1}} 1_{[r_{t+1} > \ln(\frac{K}{S_t})]} \right] \\ &= E_t^{Q^{nd}} \left[ \frac{1 + \gamma_{3t} 1_{[r_{t+1} < -\kappa_t]}}{1 + \gamma_{3t} E_t^{Q^{nd}} [1_{[r_{t+1} < -\kappa_t]}]} e^{r_{t+1}} 1_{[r_{t+1} > \ln(\frac{K}{S_t})]} \right] \\ &= \frac{E_t^{Q^{nd}} \left[ e^{r_{t+1}} 1_{[r_{t+1} > \ln(\frac{K}{S_t})]} \right] + \gamma_{3t} 1_{[\ln(\frac{K}{S_t}) < -\kappa_t]} E_t^{Q^{nd}} \left[ e^{r_{t+1}} 1_{[\ln(\frac{K}{S_t}) < r_{t+1} < -\kappa_t]} \right]}{1 + \gamma_{3t} \Phi(C_t)} \end{aligned}$$

$$\begin{aligned} E_t^{Q^{nd}} \left[ e^{r_{t+1}} 1_{[r_{t+1} > \ln(\frac{K}{S_t})]} \right] &= \int_{\ln(\frac{K}{S_t})}^{\infty} \frac{\exp \left( -\frac{1}{2} \frac{(r_{t+1} - a_{1,t})^2}{\bar{h}_t} + r_{t+1} \right)}{\sqrt{2\pi \bar{h}_t}} dr_{t+1} \\ &= \left( 1 - \Phi \left( m_t - \sqrt{\bar{h}_t} \right) \right) \end{aligned}$$

For ease of presentation  $v_t = e^{a_{1,t}^2 - (a_{1,t} + \bar{h}_t)^2}$

$$E_t^{Q^{nd}} \left[ e^{r_{t+1}} 1_{[\ln(\frac{K}{S_t}) < r_{t+1} < -\kappa_t]} \right] = v_t \left( \Phi(C_t - \sqrt{\bar{h}_t}) - \Phi(m_t - \sqrt{\bar{h}_t}) \right)$$

$$\begin{aligned} &E_t^Q \left[ e^{r_{t+1}} 1_{[r_{t+1} > \ln(\frac{K}{S_t})]} \right] \\ &= v_t \frac{\left( 1 - \Phi(m_t - \sqrt{\bar{h}_t}) \right) + \gamma_{3t} 1_{[\ln(\frac{K}{S_t}) < -\kappa_t]} \left( \Phi(C_t - \sqrt{\bar{h}_t}) - \Phi(m_t - \sqrt{\bar{h}_t}) \right)}{1 + \gamma_{3t} \Phi(C_t)} \\ &= v_t \left\{ \frac{1 - \Phi(m_t - \sqrt{\bar{h}_t})}{1 + \gamma_{3t} \Phi(C_t)} 1_{[\ln(\frac{K}{S_t}) \geq -\kappa_t]} + \frac{1 + \gamma_{3t} \Phi(C_t - \sqrt{\bar{h}_t}) - (1 + \gamma_{3t}) \Phi(m_t - \sqrt{\bar{h}_t})}{1 + \gamma_{3t} \Phi(C_t)} 1_{[\ln(\frac{K}{S_t}) < -\kappa_t]} \right\} \end{aligned}$$

$$\begin{aligned}
& e^{rf} (1 + \gamma_{3t} \Phi(C_t)) \times C_m(e_t, h_t, \gamma_{1t}, \gamma_{2t}) \\
= & \begin{cases} (1 - \Phi(m_t - \sqrt{h_t})) v_t S_t - (1 - \Phi(m_t)) K & \text{if } \ln\left(\frac{K}{S_t}\right) \geq -\kappa_t \\ (1 + \gamma_{3t} \Phi(C_t - \sqrt{h_t}) - (1 + \gamma_{3t}) \Phi(m_t - \sqrt{h_t})) v_t S_t - (1 + \gamma_{3t} \Phi(C_t) - (1 + \gamma_{3t}) \Phi(m_t)) K & \text{if } \ln\left(\frac{K}{S_t}\right) < -\kappa_t \end{cases}
\end{aligned}$$

$$\begin{aligned}
& e^{rf} (1 + \gamma_{3t} \Phi(C_t)) \times C_m(e_t, h_t, \gamma_{1t}, \gamma_{2t}) \\
= & \Phi(\sqrt{h_t} - D_t) \tilde{S}_t - \Phi(-D_t) K \\
& + \tilde{\gamma}_{3t} \left[ (\Phi(C_t - \sqrt{h_t}) - \Phi(D_t - \sqrt{h_t})) \tilde{S}_t - (\Phi(C_t) - \Phi(D_t)) K \right]
\end{aligned}$$

where

$$D_t \equiv \frac{\ln\left(\frac{K}{S_t}\right) - a_{1,t}}{\sqrt{h_t}}; \quad \tilde{S}_t \equiv e^{-\bar{h}_t(2a_{1,t} + \bar{h}_t)} S_t; \quad \tilde{\gamma}_{3t} \equiv \gamma_{3t} 1_{\left[\ln\left(\frac{K}{S_t}\right) < -\kappa_t\right]}$$

## A.4 Simulating risk-neutral returns in the presence of disappointment aversion

To evaluate option prices with maturity  $\tau > 1$ , we consider three simulation strategies, corresponding to simulation under (i) the disappointment-averse risk-neutral measure  $\mathbf{Q}$ , (ii) a no-disappointment risk-neutral measure  $\mathbf{Q}^{nd}$ , and (iii) the physical measure  $\mathbf{P}$ . Below, we provide the detailed steps for each method.

### Simulation under $\mathbf{Q}$ : Mixture of Gaussian and truncated Gaussian

Under the full disappointment-averse risk-neutral measure  $\mathbf{Q}$ , return innovations are sampled from a mixture of Gaussian and truncated Gaussian distributions.

#### Algorithm Steps:

1. Simulate:

- $\hat{z}^{\mathbf{Q}} \in \mathbb{R}^{N \times \tau} \sim \mathcal{N}(0, 1)$
- $\hat{U}_1^{\mathbf{Q}}, \hat{U}_2^{\mathbf{Q}} \in \mathbb{R}^{N \times \tau} \sim \mathcal{U}(0, 1)$

2. Initialize:

$$\tilde{e}_t^{(j)} = \tilde{e}_t, \quad h_t^{(j)} = h_t, \quad \tilde{\gamma}_{1t}^{(j)} = \tilde{\gamma}_{1t}, \quad \bar{h}_t^{(j)} = \bar{h}_t \quad \text{for } j = 1, \dots, N$$

3. For  $i = 0$  to  $\tau - 1$ , and for each  $j = 1, \dots, N$ , recursively update:

(a) Compute:

$$\begin{aligned}
e_{t+i}^{(j)} &= r_f + \left( \lambda - \frac{1}{2} \right) h_{t+i}^{(j)} + \tilde{e}_{t+i}^{(j)} \\
\gamma_{2t+i}^{(j)} &= \frac{1}{2} \left( \frac{1}{h_{t+i}^{(j)}} - \frac{1}{\bar{h}_{t+i}^{(j)}} \right)
\end{aligned}$$

(b) Compute bounds for  $\gamma_{1t+i}^{(j)}$ :

$$\hat{\gamma}_{1t+i}^{l(j)} = \frac{1}{\bar{h}_{t+i}^{(j)}} \log \left( \frac{\Phi(-C)}{\Phi(-C + \sqrt{\bar{h}_{t+i}^{(j)}})} \right),$$

$$\hat{\gamma}_{1t+i}^{u(j)} = \frac{1}{\bar{h}_{t+i}^{(j)}} \log \left( \frac{\Phi(C)}{\Phi(C - \sqrt{\bar{h}_{t+i}^{(j)}})} \right)$$

(c) Compute  $\gamma_{1t+i}^{(j)}$  using interpolated transformation:

$$\gamma_{1t+i}^{(j)} = \frac{r_f - \frac{e_{t+i}^{(j)}}{1 - 2\gamma_{2t+i}^{(j)} h_{t+i}^{(j)}}}{\bar{h}_{t+i}^{(j)}} - \frac{1}{2} + \hat{\gamma}_{1t+i}^{l(j)} \hat{\gamma}_{1t+i}^{u(j)} \cdot \left( \frac{\exp(-\tilde{\gamma}_{1t+i}^{(j)}) - 1}{\hat{\gamma}_{1t+i}^{u(j)} \exp(-\tilde{\gamma}_{1t+i}^{(j)}) - \hat{\gamma}_{1t+i}^{l(j)}} \right)$$

(d) Compute:

$$a_{1,t+i}^{(j)} = \frac{\gamma_{1t+i}^{(j)} h_{t+i}^{(j)} + e_{t+i}^{(j)}}{1 - 2\gamma_{2t+i}^{(j)} h_{t+i}^{(j)}}, \quad \kappa_{t+i}^{(j)} = - \left[ \left( \gamma_{1t+i}^{(j)} + \frac{e_{t+i}^{(j)}}{h_{t+i}^{(j)}} \right) \bar{h}_{t+i}^{(j)} + C \sqrt{\bar{h}_{t+i}^{(j)}} \right]$$

(e) Compute the truncation boundary in standard normal form:

$$\bar{\kappa}_{t+i}^{(j)} = \frac{\kappa_{t+i}^{(j)} + a_{1,t+i}^{(j)}}{\sqrt{\bar{h}_{t+i}^{(j)}}}$$

(f) Compute mixing probability  $\rho_{t+i}^{(j)}$ :

$$\rho_{t+i}^{(j)} = \begin{cases} \frac{\gamma_{3t+i}^{(j)} \Phi(C)}{1 + \gamma_{3t+i}^{(j)} \Phi(C)}, & \text{if } \gamma_{3t+i}^{(j)} > 0 \\ \frac{-\gamma_{3t+i}^{(j)} (1 - \Phi(C))}{1 + \gamma_{3t+i}^{(j)} \Phi(C)}, & \text{if } \gamma_{3t+i}^{(j)} \leq 0 \end{cases}$$

(g) Sample from truncated or non-truncated:

$$T\hat{z}_{t+i+1}^{(j)} = \begin{cases} \Phi^{-1} \left( \hat{U}_1^{\mathbf{Q}}(j, i+1) \cdot \Phi(-\bar{\kappa}_{t+i}^{(j)}) \right), & \text{if } \gamma_{3t+i}^{(j)} > 0 \\ \Phi^{-1} \left( \hat{U}_1^{\mathbf{Q}}(j, i+1) \cdot \Phi(\bar{\kappa}_{t+i}^{(j)}) + \Phi(-\bar{\kappa}_{t+i}^{(j)}) \right), & \text{if } \gamma_{3t+i}^{(j)} \leq 0 \end{cases}$$

$$T\bar{r}_{t+i+1}^{(j)} = a_{1,t+i}^{(j)} + \sqrt{\bar{h}_{t+i}^{(j)}} \cdot T\hat{z}_{t+i+1}^{(j)}$$

$$\bar{r}_{t+i+1}^{(j)} = a_{1,t+i}^{(j)} + \sqrt{\bar{h}_{t+i}^{(j)}} \cdot \hat{z}^{\mathbf{Q}}(j, i+1)$$

(h) Generate return using the mixture:

$$r_{t+i+1}^{(j)} = T\bar{r}_{t+i+1}^{(j)} \cdot \mathbb{I} \left[ \hat{U}_2^{\mathbf{Q}}(j, i+1) \leq \rho_{t+i}^{(j)} \right] + \bar{r}_{t+i+1}^{(j)} \cdot \mathbb{I} \left[ \hat{U}_2^{\mathbf{Q}}(j, i+1) > \rho_{t+i}^{(j)} \right]$$

(i) Back out the implied shock:

$$\hat{z}(j, i+1) = \frac{r_{t+i+1}^{(j)} - e_{t+i}^{(j)}}{\sqrt{h_{t+i}^{(j)}}}$$

(j) Update latent variables using:

$$\begin{aligned}
h_{t+i+1}^{(j)} &= \beta_0 + \beta_1 h_{t+i}^{(j)} + \beta_2 \left( \hat{z}(j, i+1) - \theta \sqrt{h_{t+i}^{(j)}} \right)^2 \\
\tilde{e}_{t+i+1}^{(j)} &= \alpha_0 + \alpha_1 \tilde{e}_{t+i}^{(j)} + \alpha_2 \sqrt{h_{t+i}^{(j)}} \cdot \hat{z}(j, i+1) \\
\tilde{\gamma}_{1t+i+1}^{(j)} &= \bar{\alpha}_0 + \bar{\alpha}_1 \tilde{\gamma}_{1t+i}^{(j)} + \bar{\alpha}_2 \hat{z}(j, i+1) \\
\bar{h}_{t+i+1}^{(j)} &= \bar{\beta}_0 + \bar{\beta}_1 \bar{h}_{t+i}^{(j)} + \bar{\beta}_2 \left( \hat{z}(j, i+1) - \bar{\theta} \sqrt{\bar{h}_{t+i}^{(j)}} \right)^2
\end{aligned}$$

This method requires the most elaborate sampling strategy but directly reflects the structure of the disappointment-averse risk-neutral distribution.

### Simulation under $\mathbf{Q}^{nd}$ : Gaussian dynamics with DA adjustment

Under the no-disappointment risk-neutral measure  $\mathbf{Q}^{nd}$ , return dynamics are Gaussian and the disappointment aversion enters as a Radon-Nikodym correction. This method avoids mixture sampling and provides numerical stability.

#### Option pricing formula:

$$OP_{t,\tau} = e^{-r_f \tau} \cdot \mathbb{E}_t^{\mathbf{Q}^{nd}} \left[ g(S_{t+\tau}) \cdot \prod_{i=1}^{\tau} PK_{t+i}^{\mathbf{Q}^{nd} \rightarrow \mathbf{Q}} \right] \quad (18)$$

#### Simulation Steps:

1. Simulate:

$$\hat{z}^{\mathbf{Q}^{nd}} \in \mathbb{R}^{N \times \tau} \sim \mathcal{N}(0, 1), \quad \text{set constant } C_t = C$$

2. Initialize:

$$\tilde{e}_t^{(j)} = \tilde{e}_t, \quad h_t^{(j)} = h_t, \quad \tilde{\gamma}_{1t}^{(j)} = \tilde{\gamma}_{1t}, \quad \bar{h}_t^{(j)} = \bar{h}_t$$

3. For  $i = 0$  to  $\tau - 1$ , and for each  $j$ :

(a) Compute:

$$\begin{aligned}
e_{t+i}^{(j)} &= r_f + (\lambda - \frac{1}{2}) h_{t+i}^{(j)} + \tilde{e}_{t+i}^{(j)} \\
\gamma_{2t+i}^{(j)} &= \frac{1}{2} \left( \frac{1}{h_{t+i}^{(j)}} - \frac{1}{\bar{h}_{t+i}^{(j)}} \right)
\end{aligned}$$

(b) Compute bounds for  $\gamma_{1t+i}^{(j)}$ :

$$\begin{aligned}
\hat{\gamma}_{1t+i}^{l(j)} &= \frac{1}{\bar{h}_{t+i}^{(j)}} \log \left( \frac{\Phi(-C)}{\Phi(-C + \sqrt{\bar{h}_{t+i}^{(j)}})} \right) \\
\hat{\gamma}_{1t+i}^{u(j)} &= \frac{1}{\bar{h}_{t+i}^{(j)}} \log \left( \frac{\Phi(C)}{\Phi(C - \sqrt{\bar{h}_{t+i}^{(j)}})} \right)
\end{aligned}$$

(c) Compute  $\gamma_{1t+i}^{(j)}$  using the interpolated form (same as in A.1)

(d) Compute:

$$a_{1,t+i}^{(j)} = \frac{\gamma_{1t+i}^{(j)} h_{t+i}^{(j)} + e_{t+i}^{(j)}}{1 - 2\gamma_{2t+i}^{(j)} h_{t+i}^{(j)}}$$

$$\kappa_{t+i}^{(j)} = - \left[ \left( \gamma_{1t+i}^{(j)} + \frac{e_{t+i}^{(j)}}{h_{t+i}^{(j)}} \right) \bar{h}_{t+i}^{(j)} + C \sqrt{\bar{h}_{t+i}^{(j)}} \right]$$

(e) Compute transformed shock:

$$\hat{z}(j, i+1) = \sqrt{\frac{\bar{h}_{t+i}^{(j)}}{h_{t+i}^{(j)}}} \cdot \hat{z}^{\mathbf{Q}^{nd}}(j, i+1) + \frac{\gamma_{1t+i}^{(j)} \bar{h}_{t+i}^{(j)} + \frac{\bar{h}_{t+i}^{(j)}}{h_{t+i}^{(j)}} e_{t+i}^{(j)} - e_{t+i}^{(j)}}{\sqrt{h_{t+i}^{(j)}}}$$

(f) Generate return:

$$r_{t+i+1}^{(j)} = e_{t+i}^{(j)} + \sqrt{h_{t+i}^{(j)}} \cdot \hat{z}(j, i+1)$$

(g) Compute the DA adjustment kernel:

$$PK_{t+i+1}^{\mathbf{Q}^{nd} \rightarrow \mathbf{Q}(j)} = \frac{1 + \gamma_{3t+i}^{(j)} \cdot \mathbb{I} \left[ r_{t+i+1}^{(j)} < -\kappa_{t+i}^{(j)} \right]}{1 + \gamma_{3t+i}^{(j)} \cdot \Phi(C)}$$

(h) Update latent variables (as in A.1).

### Simulation under P: Physical measure with full kernel

This strategy simulates return paths under the physical measure and applies the full pricing kernel to adjust for risk and disappointment aversion.

### Option pricing formula:

$$OP_{t,\tau} = e^{-r_f \tau} \cdot \mathbb{E}_t^{\mathbf{P}} \left[ g(S_{t+\tau}) \cdot \prod_{i=1}^{\tau} PK_{t+i} \right] \quad (19)$$

### Simulation steps:

1. Simulate:

$$\hat{z} \in \mathbb{R}^{N \times \tau} \sim \mathcal{N}(0, 1), \quad \text{set } C_t = C$$

2. Initialize:

$$\tilde{e}_t^{(j)} = \tilde{e}_t, \quad h_t^{(j)} = h_t, \quad \tilde{\gamma}_{1t}^{(j)} = \tilde{\gamma}_{1t}, \quad \bar{h}_t^{(j)} = \bar{h}_t$$

3. For  $i = 0$  to  $\tau - 1$ , and for each  $j$ :

(a) Compute:

$$r_{t+i+1}^{(j)} = e_{t+i}^{(j)} + \sqrt{h_{t+i}^{(j)}} \cdot \hat{z}(j, i+1)$$

compute  $\kappa_{t+i}^{(j)}$  and all gamma terms as in A.1



(b) Compute the full pricing kernel:

$$PK_{t+i+1}^{(j)} = \frac{\exp\left(\gamma_{1t+i}^{(j)} r_{t+i+1}^{(j)} + \gamma_{2t+i}^{(j)} (r_{t+i+1}^{(j)})^2\right) \cdot \left(1 + \gamma_{3t+i}^{(j)} \cdot \mathbb{I}[r_{t+i+1}^{(j)} < -\kappa_{t+i}^{(j)}]\right)}{\left(1 + \gamma_{3t+i}^{(j)} \Phi(C)\right) \cdot \sqrt{1 - 2h_{t+i}^{(j)} \gamma_{2t+i}^{(j)}} \cdot \exp\left(\frac{2\gamma_{2t+i}^{(j)} (e_{t+i}^{(j)})^2 + 2\gamma_{1t+i}^{(j)} e_{t+i}^{(j)} + h_{t+i}^{(j)} (\gamma_{1t+i}^{(j)})^2}{2(1 - 2\gamma_{2t+i}^{(j)} h_{t+i}^{(j)})}\right)}$$

(c) Update all latent variables (as in A.1).

## A.5 Extracting the empirical pricing kernel

### Risk neutral density

We implement the method of [Breedon and Litzenberger \(1978\)](#) to recover the RN density from option prices. The following steps detail the construction of the density:

1. For a fixed trading day  $t$  and maturity  $\tau$ , collect put option quotes with positive bid and ask prices:

$$\text{bid}_i > 0, \quad \text{ask}_i > 0.$$

2. Filter out options with excessive effective spreads:

$$\frac{\text{ask}_i - \text{bid}_i}{(\text{ask}_i + \text{bid}_i)/2} \leq 0.75.$$

3. Ensure monotonicity in observed put prices  $P(K)$  by removing price outliers that violate:

$$P(K_{i+1}) \geq P(K_i).$$

4. Augment the data with two synthetic points for numerical stability:

$$P(100) = 0, \quad P(2S) = S.$$

Note that the value of the SPX on 1996-01-01 was 620.73 and on 2021-12-31 it was 4766.18. It is unlikely that  $P(100)$  is far removed from 0.

5. Retain only those maturities with at least four valid option contracts and at least one with  $K > S$ .

6. Fit a smooth spline  $\hat{P}(K)$  through the mid-quotes of the put option prices as a function of strike  $K$ .

7. Approximate the discrete RN probabilities:

$$p(K_i) = \hat{P}(K_i + 1) - \hat{P}(K_i).$$

8. Expand the strike support until:

$$\min p(K_i) < 0.005.$$

9. Compute the log return implied by each strike:

$$r_i = \log\left(\frac{K_i}{S}\right).$$

10. Construct the RN density over the log return grid using discrete differences:

$$f_Q(r_i) = \frac{p(r_{i+1}) - p(r_i)}{r_{i+1} - r_i}.$$

## Estimating the physical distribution from GARCH simulations

We simulate returns under the physical measure using a GARCH model estimated on historical log returns. The procedure is as follows:

1. Estimate a GARCH-type model (e.g., EGARCH or GRJ-GARCH) for log returns  $r_t$  and simulate future returns  $\{r_{t+1}^{(s)}\}_{s=1}^S$  over  $\tau$ -day horizon.
2. Define  $N \approx 50$  bins over the support  $[r_{\min}, r_{\max}]$  from the simulated log returns at ma.
3. Let  $b_j$  be the midpoint of bin  $j$  and define the empirical density:

$$f_P(b_j) = \frac{1}{S \cdot w_j} \sum_{s=1}^S \mathbf{1}_{r_{t+1}^{(s)} \in \text{bin}_j},$$

where  $w_j$  is the width of bin  $j$ .

4. Rescale the density to remove simulated returns falling outside the RN support, redistributing excess mass proportionally across remaining bins:

$$f_P^*(b_j) = \frac{f_P(b_j)}{\sum_{j \in \mathcal{R}} f_P(b_j)} \quad \text{for } j \in \mathcal{R},$$

where  $\mathcal{R}$  is the restricted range of the RN distribution.

5. Interpolate the RN density  $f_Q(r)$  at the bin midpoints  $\{b_j\}$  using linear interpolation.
6. Standardize the log returns  $b_j$  using the standard deviation  $\sigma_P$  of the simulated distribution:

$$r_j^{\text{std}} = \frac{b_j}{\sigma_P}.$$

This procedure yields matched RN and physical densities over a common support, allowing for direct calculation of the pricing kernel as:

$$\log PK(r) = \log f_Q(r) - \log f_P(r).$$

## A.6 Tables

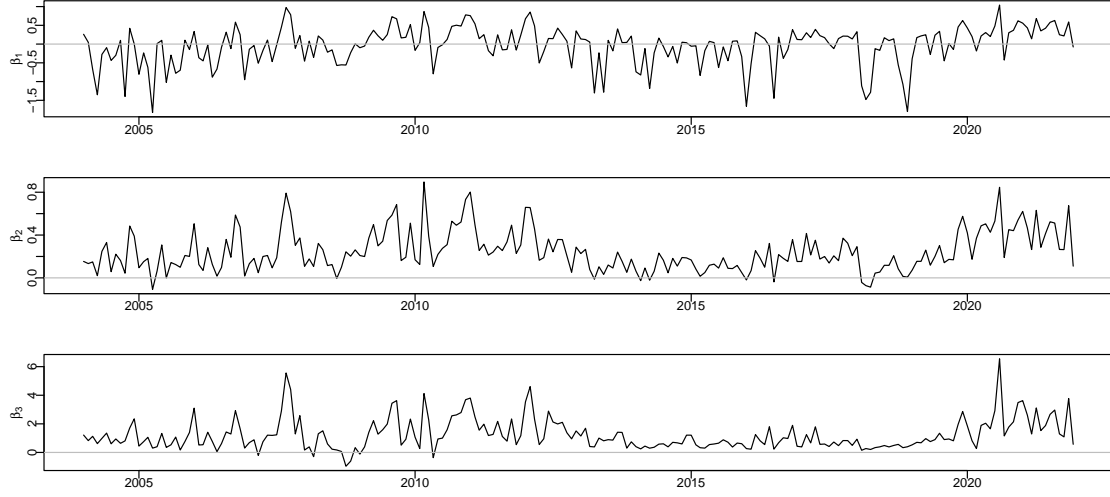
Table 8: The pricing kernel and DA (Annual regressions)

Year	$r_t$	$r_t^2$	DA	$R^2$	$R^2_{\text{no DA}}$	Year	$r_t$	$r_t^2$	DA	$R^2$	$R^2_{\text{no DA}}$
2004	-0.036*** (-2.77)	0.029*** (6.71)	0.431*** (10.2)	0.37	0.33	2013	0.06*** (6.99)	0.042*** (16.05)	0.83*** (29.04)	0.3	0.22
2005	0.037** (2.48)	0.011** (2.15)	0.46*** (10.44)	0.23	0.18	2014	-0.102*** (-13.09)	0.057*** (22.02)	0.593*** (23.88)	0.49	0.45
2006	0.124*** (7.92)	0.058*** (11.13)	0.61*** (12.37)	0.22	0.15	2015	-0.056*** (-6.94)	0.037*** (13.93)	0.467*** (18.1)	0.32	0.29
2007	0.138*** (8.36)	0.084*** (20.47)	0.654*** (11.06)	0.24	0.21	2016	0.018*** (2.87)	0.092*** (48.25)	0.768*** (37.27)	0.45	0.38
2008	-0.147*** (-9.94)	0.022*** (7.09)	0.002 (0.04)	0.37	0.37	2017	-0.001 (-0.21)	0.156*** (113.22)	0.866*** (65.7)	0.62	0.55
2009	0.099*** (6.97)	0.078*** (24.62)	0.466*** (8.91)	0.41	0.4	2018	-0.094*** (-19.24)	0.018*** (10.47)	0.392*** (26.12)	0.31	0.29
2010	0.178*** (13.04)	0.098*** (30.19)	0.652*** (13.27)	0.4	0.36	2019	0.101*** (22.9)	0.118*** (83.74)	0.707*** (47.86)	0.38	0.32
2011	0.1*** (6.52)	0.083*** (22.97)	0.589*** (10.64)	0.33	0.31	2020	0.191*** (37.53)	0.123*** (106.94)	0.622*** (33.12)	0.48	0.45
2012	0.189*** (19.25)	0.079*** (32.6)	0.979*** (26.97)	0.33	0.24	2021	0.263*** (65.73)	0.131*** (129.09)	0.725*** (48.45)	0.59	0.55

This table reports the results of annual regressions of the log pricing kernel on standardized return quantiles, estimated separately for each year from 2004 to 2021. The dependent variable is the log pricing kernel, defined as the logarithm of the ratio between the risk-neutral and physical return densities. Risk-neutral densities are extracted from CBOE option prices with maturities fixed at 25 days, following [Breedon and Litzenberger \(1978\)](#), by applying the second derivative to a smooth spline fitted to put prices. Physical return densities are obtained by simulating returns from an EGARCH(2,2)-in-mean (2,2) model estimated on SPX returns. Return quantiles are standardized by the standard deviation of the simulated distribution. The regression includes the standardized return  $r_t^*$ , its square  $(r_t^*)^2$ , a disappointment aversion indicator  $\mathbb{I}[r_t^* < -C_t]$ , and time fixed effects. Reported are the coefficient estimates and their associated  $t$ -statistics (in parentheses).  $R^2$  values are provided for both the full specification and a restricted version without the DA component. Statistical significance at the 10%, 5%, and 1% levels is denoted by \*, \*\*, and \*\*\*, respectively.

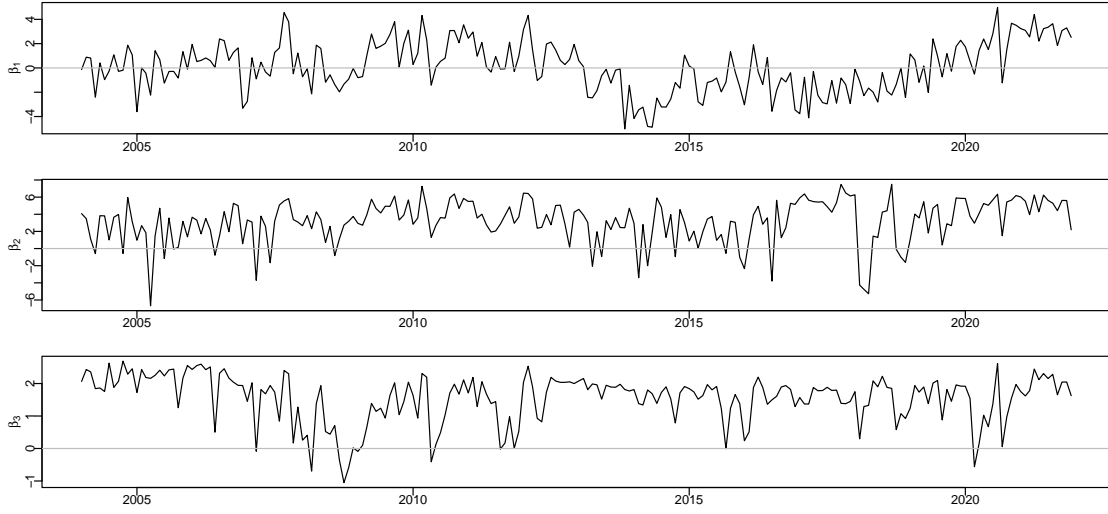
## A.7 Figures

Figure 15: Regressions log pricing kernel



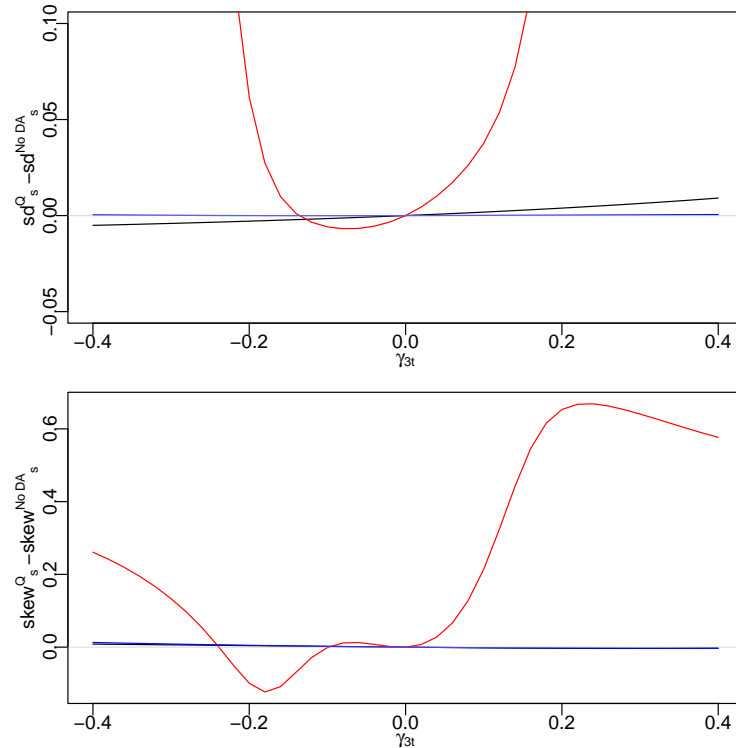
These figures display the coefficient estimates from the regressions described in Equation (5). Each day, we regress the logarithm of the empirical pricing kernel, extracted from SPX options with maturities closest to 30 days, on a constant, the standardized return  $r_i^*$ , its non-centered square  $(r_i^* - a)^2$ , and a DA indicator. The estimated coefficients are averaged within each month and plotted. The fourth panel shows the incremental explanatory power of the DA component, measured as the difference in  $R^2$  between the full regression in Equation (5) and a restricted version that excludes the DA term. The physical densities are constructed by estimating an EGARCH(2,2) model with an in-mean ARMA(2,2) specification on SPX returns, and simulating the corresponding conditional return distribution. Simulated returns are grouped into 50 equally sized intervals to approximate the density, and return quantiles are standardized by the standard deviation of the simulated physical distribution. The RN densities are derived from CBOE option data using contracts with closest to 30 day for that date, following [Breedon and Litzenberger \(1978\)](#).

Figure 16: T-statistics: daily regressions (5)



These figures display the  $t$ -statistics from the regressions described in Equation (5). Each day, the logarithm of the empirical pricing kernel, extracted from SPX options with maturities closest to 30 days, is regressed on a constant, the standardized return  $r_i^*$ , its non-centered square  $(r_i^* - a)^2$ , and a DA indicator. The  $t$ -statistics are averaged within each month and plotted.

Figure 17: Term structure RN densities vs No DA density



The figure depicts the wedge between the standard deviation and skewness of the DA RN and no DA RN distributions over 180-day terms as a function of  $\gamma_{3t}$ . The upper panel show the average wedge across terms for the standard deviation and the lower panel for the skewness. To simulate the physical distribution, we use an EGARCH(2,2)-in-mean(2,2) model. The results are shown for three different values of  $C_t = \{-1.5, 0, 1.5\}$ .